THEORETICAL STUDIES OF STRUCTURE AND DYNAMICS OF

CHALCOGENIDE GLASSES

A thesis presented to

the faculty of

the College of Arts & Sciences of Ohio University

In partial fulfillment

of the requirements for the degree

Doctor of Philosophy

Fakharul Inam

November 2009

This thesis entitled

THEORETICAL STUDIES OF STRUCTURE AND DYNAMICS OF

CHALCOGENIDE GLASSES

by

FAKHARUL INAM

has been approved for

the Department of Department of Physics & Astronomy

and the College of Arts Sciences by

David. A. Drabold

Distinguished Professor of Physics

Benjamin M. Ogles

Dean, College of Arts & Sciences

INAM, FAKHARUL, Ph.D., November 2009, Department of Physics & Astronomy

<u>Theoretical Studies of Structure and Dynamics of Chalcogenide Glasses</u> (101 pp.)

Director of Thesis: David A Drabold

In this work, the structural and dynamical properties of Ge-Se and Ag-Ge-Se glasses, using first principle molecular dynamics simulations, is presented. Raman and calorimetric studies on $Ge_X Se_{1-x}$ glasses have provided evidence for the existence of the intermediate phase (IP) in chalcogenides and other glasses. Here we thoroughly discuss the *ab-initio* models of $Ge_X Se_{1-x}$ glasses over a wide composition range and provide an atomistic picture of the IP. A thorough analysis of our models reveals that the IP in these glasses may arise from the competition between amorphous $GeSe_2$ and a polymeric a-Se phases, which gives rise to the non-monotonic evolution (a topological feature of the IP) of the network parameters through the IP window. A qualitative comparison is made between the topological features extracted from the models and the experiments. A possible electronic signature of the IP in terms of the shift in the conduction edge energy in the IP range is predicted. The results agree with the shift in the white line position for the Se atoms in the K-edge X-Ray Absorption Near Edge Structure (XANES) spectra.

A microscopic picture of the silver dynamics in $GeSe_3$:Ag glass is presented. The dynamics of Ag is explored at two temperatures: 300K and 700K. In the relaxed $GeSe_3$ glass network, it is shown that the Ag occupies *trapping centers* (TC) that exist between pairs of suitably separated host sites. The charge state of the Ag in the

glass network is computed and it is shown that Ag is neutral if weakly bonded and is Ag$^+$ if in a trapping center. The dynamics of the Ag is shown to be largely effected by the neighboring host sties. At room temperature, Ag is mainly trapped at the TC with small hopping probability between neighboring TCs. At higher temperature (700 K), the Ag motion is diffusive and is proceeded via a trapping-release dynamics between *supertraps* or cages consisting of multiple trapping center sites in a small volume. Our work offers a first-principles identification of trapping centers invoked in current theories, with a description of their properties and associated Ag dynamics. The understanding of the Ag dynamics in bulk glass is exploited to model the surface of a solid electrolyte (GeSe$_3$:Ag).

Finally, the topological-electronic correlations, previously reported in the realistic models of a-Si [13], are explored further. It is demonstrated that analogous correlations exist in amorphous SiO$_2$ and in the organic molecule β-carotene, which hints towards the universal character of these correlations.

Approved: _____

David A Drabold

Distinguished Professor of Physics

Dedicated to Ammi (Mom) and Abbu (Dad)

Acknowledgments

"I can no other answer make but thanks/And thanks; and ever thanks."

<div align="right">

- Shakespeare's *Twelfth Night*

</div>

Like Sebastian from the *Twelfth Night*, I find myself with no other word but thanks at the conclusion of another chapter in my academic life. There is a long list of people and I am not going to make an attempt to thank all of them. It is the word which is scarce, not the gratitude.

This work is carried out under the supervision of Prof. Drabold. As a supervisor, he has been very kind and careful in letting me explore things without putting too many constraints. He kept a watchful eye on the scientific conclusions I have drawn and did not let go even simple ideas unappreciated. As a mentor, he has been very keen in pointing out career opportunities and helping me find directions for a career in physics. Its been a wonderful time listening to and discussing with him, physics and the politics surrounding the subject. The better way to thank him is to pay forward what I have learned from him. I am looking forward for a long collaboration in future.

I benefitted in my work from the *simulated* discussions with the group members, Dr. Mingliang Zhang, Dr. Indira Chaudhury, Sudeshna, Yue, Bin and Tesfaye. I am grateful to them, specially to my friend Tesfaye for the wonderful time we spent discussing, physics and what not. I am also thankful to Dr. Gang Chen for providing me an opportunity to take part in the XANES measurements, closely related to

Table of Contents

List of Figures

List of Tables

CHAPTER 1

Introduction

Liquid, when cooled down, either *discontinuously* solidifies to a crystalline (topo-
logically ordered) phase or goes through a *continuous* phase transition and solidifies
to a metastable disordered solid generally named as an *amorphous* phase. The liquid-
crystal transition can be identified as the discontinuous drop in the volume V(T) of
the system at a critical temperature with sufficiently slow quench rate. Fast quench-
ing of the liquid mostly results in a continuous decrease in the volume until the slope
drops to a lower value when the temperature passes a threshold known as the *glass
transition* temperature T_g. The disordered solids obtained through a glass transition
are generally categorized as *glasses* [1]. Thermodynamically, a glass phase is reached
when the system becomes *non-ergodic* due to the continuous slowing down of one or
more of its degrees of freedoms [2]. Glasses can generally be classified in terms of the
type of bonding between constituent atoms. In this study the focus is on covalent
glasses (chalcogenides Ge_xSe_{1-x} and SiO_2) and amorphous system (a-Si).

All though the atomic structure of the glass is quite similar to that of crystalline
at the nearest neighbor distances, it becomes random at higher lengths and thus
show no translational symmetry. The continuous random network (CRN) model,
first proposed by Zachariasen [3], is generally accepted as the structural model for
the covalent glasses. The model assumes the same nearest neighbor distances as that

in crystalline phase and allows the topological disorder in terms of the broadening in the bond angle distribution. The nearest neighbor structure of the covalently bonded glass network is generally studied using the 8-n rule, where 'n' is the valence number. The underlying principle is that the atomic configuration, which ensures the complete outer shells (8 electrons) of atoms, is the most stable configuration. This suggestion was put forward by Mott [4] to explain the lesser insensitivity to impurities shown by chalcogenide glasses (glasses containing elements from column VI: S, Se and Te), which is in contrast with the crystalline semiconductors. The 8-n rule ensures that the outer shell of all the constituent atoms is full. The rule explains the glass forming tendency of chalcogenides over a wide range of binary and ternary compositions [5].

Absence of the translation symmetry greatly effects the electronic properties of the system. Anderson addressed the problem of electronic diffusion on a disordered lattice and showed that the electronic states become *localized* (Anderson Localization) in the presence of lattice disorder. He treated the disorder in terms of the random potential wells seen by the diffusing electron [6]. The exponential nature of the electronic density of states at the band edges for disordered systems, first observed by Urbach [7], is a direct consequence of the topological disorder. The *realistic* models of glasses [8][9] and amorphous systems [97][11] localized band tail states which couple strongly to the lattice vibrations [12]. Recently in a-Si, a topologically correlated network of anomalous bond lengths is reported which is shown to be responsible for the exponential band tails [13][14].

1.1 Chalcogenide Ge_xSe_{1-x} Glasses

The chalcogenide glasses have been widely studied for their structural, optical and electronic properties. Their industrial use include fiber optics [15], phase change memories [16], optical recording [17], and non volatile memory devices [18]. The Ge_xSe_{1-x} glassy alloys, in particular, have been a focus of extensive research as their structural and electronic properties can be substantially changed by varying the Ge content 'x'. Most of the research on these glasses is focused on understanding the network properties like intermediate range order (IRO) and rigidity transition using scattering methods and calorimetric measurements etc [19][20][26]. Theoretical modeling based on *ab-initio* molecular dynamics (MD) simulations have been used successfully in studying these glasses at the atomic scale [23][24][22]. The density functional theory (DFT) [25] is used as the main theoretical tool. The glass structure is generally modeled by quenching the liquid phase (melt-quenched method), mimicking the real glass formation in the laboratory.

1.1.1 Rigidity Threshold and The Intermediate phase

The topology of the Ge-Se network, in general, is best described as links between 4-fold $Ge(Se_{1/2})_4$ tetrahedra and polymeric chains of 2-fold Se (according to the 8-n rule) forming a CRN. The addition of 4-fold Ge tetrahedra, as can easily be realized, greatly effects the topology of the network. The IRO (which is attributed to the first sharp diffraction peak (FSDP) in the static structure factor) changes considerably with
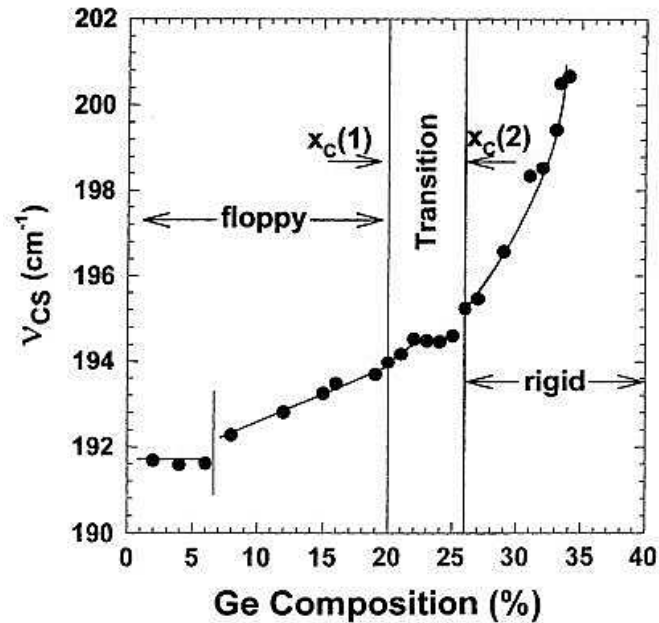
Figure 1.1: Variation of the corner shared tetrahedra raman mode with the Ge content. The IP can be identified as the *flattening* of the raman mode in the compositional window $x \in (0.20, 0.25)$. (from [40])

the Ge content [27][28][20]. On the compositional scale 'x', the network connectivity evolves from a vibrationally floppy network for x=0 (a-Se) to a rigid tetrahedral glass GeSe$_2$(network of connected GeSe tetrahedra) for x=0.33. The former has very low energy vibrational modes because of the low coordination, the latter is a rigid network glass. Looking at the two widely different network topologies at the two ends of the composition range, it is intuitive to guess some sort of structural transition occurring some where between the two end compositions.

In the early 1980s, Phillips [37][38] and Thorpe [39] had introduced the idea of rigidity percolation in network forming covalent glasses based upon the constraint theory, which predicts the floppy to rigid transition in glass networks as the bonding

constraints are added to them. The basic assumption is that the bond stretching and bond bending forces can be considered as the atomic constraints in the formation of the network. The transition occurs when the total constraints per atom equals the degrees of freedom of the system. The rigidity percolation threshold is found to exist at $\bar{r} = 2.4$ [39], where $\bar{r}$ is the mean coordination of the network. The glass forming ability of the system is conjectured to be optimum at the rigidity threshold. For Ge_xSe_{1-x}, the rigidity threshold corresponds to the composition x = 0.20. Later, based upon Raman scattering and calorimetry study, Boolchand and his group [40] identified a 'double' rigidity transition, instead of one, in Ge_xSe_{1-x} glasses (Fig. 1.1). A finite composition window $x \in (0.20, 0.25)$ between two transitions is referred to as an intermediate phase (IP). Since then, the IP is observed in a wide range of glassy alloys for example, Si_xSe_{1-x} and As_xSe_{1-x} [26].

The structural manifestations of the IP have been sought by researchers using diffraction techniques. Studies on the first sharp diffraction peak (FSDP) of the Ge-Se glasses indicated that the inverse peak position and peak area of the FSDP exhibit the telltale "flattening" in the IP composition range[27][28], also supported by anomalous X-ray scattering measurements [29]. However, recent work by Shatnawi and co-workers did not confirm these observations [20]. The latter authors also conducted high-energy x-ray diffraction and extended x-ray absorption fine structure analyses on Ge_xSe_{1-x}, but could not find structural fingerprints of the IP in the first atomic shell [20].

Little is known of possible electronic features of the IP. Taniguchi *et al.* [30] have reported photoemission (PES) and inverse photoemission (IPES) studies on these glasses. They observed a splitting of the conduction band at the first rigidity threshold with the major peak shifting towards lower energies. Recently, Novita *et al.*[31] have observed a slight increase in the conductivity of solid electrolyte glasses $(AgI)_x(AgPO3)_{1-x}$ in the IP range relative to stressed rigid phase. In the IP, glasses are found to show a number of interesting properties like absence of aging [32] and internal stress [33]. Links between the intermediate phase and protein folding [34] and high T_c superconductors [35] are also realized. The understanding of the IP at the atomic scale is thus of a general interest.

The first theoretical picture of the IP was developed by Thorpe et. al. [41]. They modified the floppy-to-rigidity transition concept by introducing the idea that in the floppy network, inclusion of extra bonding constraint originates the rigid but *stress free* regions. Thus when the system goes through the first transition, network becomes rigid but still in a stress free or isostatic state. Further inclusion of bonding constraints would result in the accumulation of stress in the network, and hence the system will go through the second transition from *stress free rigid* to *stressed rigid* transition. The isostatic state of the network in the IP range is what they referred to as the *self-organized* phase, in which the network responds to the addition of bonding constraints in a way to avoid the accumulation of stress. Simulations were performed using different empirical approaches to study the realization of self-organized state of

the network. Thorpe et. al. [41] have made attempts to achieve a stress free state, starting from a floppy network and adding constraints (bonds) in such a way to avoid 'stressed bonds'. Micoulaut and Phillips [42] used a probabilistic approach. They constructed clusters of Ge_xSe_{1-x} by using the size increasing cluster approximation (SICA). They showed that, starting from a floppy cluster, an isostatic phase can be achieved. The isostatic phase obtained from such construction shows a local minimum in the constrained-related free energy, suggesting an equilibrium phase with respect to cross-linking of these units. Other approaches have been proposed by a number of authors [43]. Though these efforts have provided valuable insights into the IP, none of these approaches undertake the realistic interactions between the atoms and do not directly relate to the experimental observables.

1.1.2 Ag-doped glases

Ge_xSe_{1-x} glasses are generally found to obey the 8-n rule [1]. A deviation from this rule, however occurs when I-group elements like Cu and Ag (n < 4) are added to chalcogenide glasses. Copper is known to have coordination number 4 [44] in $(As_{0.4}Se_{0.6})_{1-x}Cu_x$ glassy alloys while Ag shows coordination more then 2 in $GeSe_2$ glass [45][46], instead of one according to the 8-n rule. The 8-n rule is modified to allow the transfer of charge to the atoms with n < 4 such that the total number of electrons, non-bonding plus the shared electrons, in the outer shell remains 8 [47]. According to this rule, all the atoms with n < 4 should have coordination 4, which

explains the Cu coordination in $(As_{0.4}Se_{0.6})_{1-x}Cu_x$. It is interesting to note that the bond constraint theory, discussed above, does not correctly predict the glass forming compositions for $Ag_2S(Se)$ and $Cu_2S(Se)$ added As and Ge chalcogenides [48]. The glass formation for Ag-Ge-Se compositions in the IP window is found to be enhanced, suggesting a link between the IP phase in the host glass and the Ag bonding to the glass network [49]. The special interest in the Ag-Ge-Se glasses is due to their super ionic behavior for suitable Ag concentration. In $(GeSe_3)_{1-x}Ag_x$ glasses, the ionic conductivity shows an abrupt increase by a factor of about 10 for x $\approx$ 0.1 [50][51]. Such dependence on the Ag content is interpreted as a percolative transition [53][52]. In case of $(Ag_2S)_x(As_2S_3)_{1-x}$, the increase in the conductivity is found to correlate with the rigid-to-floppy transition [54]. Silver is generally introduced in the glass through photo-dissolution [55]. Photo dissolution occurs when a Ag layer is in contact with the glass: Ag diffuses into the glass network during light illumination [45]. Recently, a solid electrolyte memory device Programmable Metallization Cell (PMC) was proposed and experimentally realized; it controls the conductivity of the Ag doped Ge-Se glass by switching the voltage across it. The Ag atoms diffuse and form metallic filaments extending from one electrode to another and thus abruptly increase the conductivity of the glass. The process can be reversed by applying the reverse bias [56]. The *ab-initio* models of $Ag_x(GeSe_3)_{1-x}$ (for x = 0.1 and 0.15) are reported [58][59], which shows structural properties in good agreement with the

neutron diffraction experiment. Silver is found to be highly mobile and show hopping dynamics, though the Ag bonding to the glass network is not yet thoroughly explored.

1.1.3   This Work

This dissertation is mainly focused on developing the basic understanding of the compositional trends and incorporation of Ag and its dynamics in Ge_xSe_{1-x} glasses, using first principle methods. As discussed above, the appearance of the IP in these glasses poses fundamental questions regarding the topology of the glassy network. Using realistic models of these glassy alloys over a wide composition range, an atomistic picture of the IP is developed which suggests that the appearance of the IP is a result of the competition between a-Se and the stoichiometric $GeSe_2$ phase. A thorough topological analysis is presented to support this picture and qualitative links with the experiments are provided. Also an electronic signature of the IP is proposed which is supported by recent X-ray Absorption Near Edge Structure (XANES) measurements. The dynamics of the silver ions in a solid electrolyte $(GeSe_3)_{0.85}Ag_{0.15}$ is thoroughly discussed. The model used here is originally developed using local orbital basis code FIREBALL [60] which shows good agreement with the neutron diffraction measurements. It is relaxed using the plane-wave *ab-initio* code VASP [61] which incorporates a complete basis set. By analyzing long thermal trajectories, it is shown that Ag diffusion consists of hopping between *trapping sites*. The topology of the silver-traps is discussed and it is shown that the Ag is only weakly bonded (by transferring charge to

its neighbors) to the glass network. The higher temperature Ag dynamics resembles a percolative process as suggested by Bychkov et al. [52]. The *trapping* picture of Ag resulting from this study gives some insight into the coordination state of Ag in this glass. Ag being weakly bonded to the network can have two or more nearest neighbors. A melt-quenched surface model of $GeSe_2$ glass is presented and its structural, vibrational and electronic properties are thoroughly discussed. Using an alternate dynamical method, an example of a surface model of $(GeSe_3)_{0.9}Ag_{0.1}$ is also presented. The model shows a good example of how Ag modifies its neighboring glass network. These surface models can be used to study the light induced processes, for example Ag photo-doping. To study the strain field due to the shift in the bond lengths and bond angles in the disordered networks, a simple geometrical tool is developed and applied to a-Si and SiO_2 glass network. Topological-electronic correlations in SiO_2 glass are thoroughly discussed and compared with that of a-Si. It is found that the valence edge states are effected by the tetrahedra bond angles (O-Si-O) and conduction edge states are sensitive to the Si-O-Si angles. The effects due to Ge-Se-Ge angles on the conduction edge are also noted for the Ge_xSe_{1-x} glasses, which hints towards universality of the underlying topology of the band tail states in these glasses.

All the calculations presented in this thesis are performed within the frame work of local density approximation (LDA) DFT. The local orbital DFT code FIREBALL [60] is used in modeling the Ge-Se bulk glasses and their surfaces. The calculations on a-Si and a-SiO_2 are carried out using SIESTA [62]. The plane wave DFT code

VASP [61] is used for some calculations for liquid $GeSe_3$ model and to study the Ag dynamics in Ge-Se bulk glass. The approximations used in the work are mentioned in the chapters.

1.2 Thesis Outline

In chapter 2, the atomistic picture of the IP is thoroughly developed. Chapter 3 discusses the dynamics of Ag in $(GeSe_3)_{0.9}Ag_{0.10}$ glass. In chapter 4, a melt-quenched surface model of $GeSe_2$ glass is presented. An example of the surface of a glass $(GeSe_3)_{0.9}Ag_{0.10}$ is provided in the Appendix A. A farther insight into the topological correlations reported in a-Se models is provided in chapter 5 and similar correlations are discussed in a-SiO_2. Finally the important results of this study are summarized in chapter 6.

The work reported in this thesis is mainly contributed by me. The Ge-Se bulk models were provided by Dr. D. Tafen and the calculation of Ag charge in $(GeSe_3)_{0.9}Ag_{0.10}$ model is contributed by Dr. I. Chaudhuri. My colleague S. Chakraborty provided the eigen value spectrum for the a-SiO_2 model. The calculations of HOMO and LUMO levels for carotene-β are due to Prof. James P. Lewis. The results included in the thesis are mostly published, except results in chapter 5, which are recently submitted for the publication.

CHAPTER 2

Intermediate Phase in Ge$_x$Se$_{1-x}$

Glasses

In this chapter we present *ab initio* MD models of Ge$_x$Se$_{1-x}$ glasses over a wide composition range including the IP window. In these models, the evolution of structural parameters such as the concentrations of corner-sharing (CS) and edge-sharing (ES) tetrahedra show a non-monotonic behavior. These parameters deviate from a chemically ordered CRN, and tend to saturate in the composition range which coincides with the IP window, suggesting a link between the experiments and the models. Further we develop an atomistic picture of the IP emerging directly from models resulting from realistic atomistic simulations. We find that the IP in Ge$_x$Se$_{1-x}$ glasses emerges as a consequence of the competition between the GeSe$_2$ phase and the polymeric a-Se phase. Our work shows that MD simulations can provide essential insight into the IP. To a significant degree, our work supports the picture of Mi-
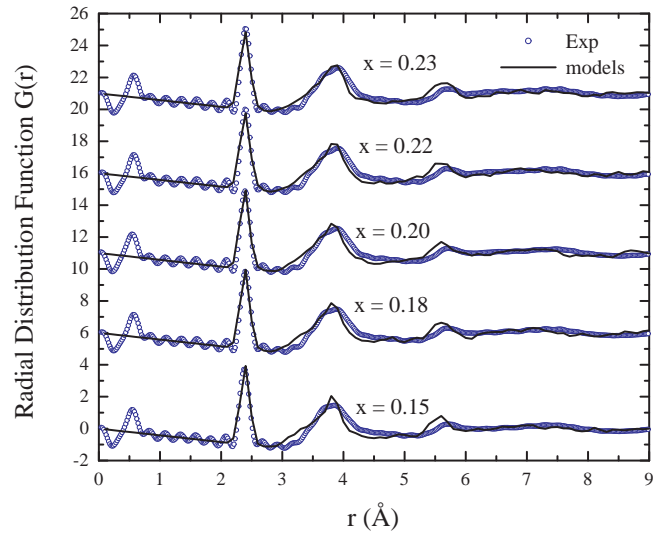
Figure 2.1: Total radial distribution function G(r), calculated from the models, for different compositions is compared with the experiment. Details of the experiments are reported in [63].

coulaut and Phillips [42], inferences of Boolchand[26], and suggests the nature of the self-organization described in Ref. [41].

2.1 Structural Models of the IP

Atomistic models of the IP were obtained using the approximate *ab initio* density functional code FIREBALL developed by Sankey and co-workers [60]. A series of 500-atom Ge_xSe_{1-x} models with Ge concentrations (x = 0.15, 0.18, 0.22, 0.23, 0.25) is generated using a quench from melt technique. Atoms were randomly placed in a cubic cell with suitable (fixed) volume. The cells were then heated to 4200 K, and

then equilibrated at 1500 K for about 3.5 ps. Then, they were quenched to 400 K over a period of about 4.5 ps, using velocity rescaling. Finally, the cells were steepest descent quenched to 0 K. Beside this series we have used models with x = 0.20 and x = 0.10 by Tafen et. al. [9] and x = 0.33 by Cobb [8]. Beside glass models, we also generated a long (75 ps) molecular dynamics trajectory of liquid GeSe$_3$ composition consisting of 96 atoms at 1200K using plane-wave **ab initio** code VASP[61] (Vienna *ab initio* simulation package) at constant volume and temperature.

The coordination states for Se and Ge in all these models are 2-fold and 4-fold respectively. A concentration of about 16-20% of under (1-fold) and over (3-fold) coordinated Se defects are observed for all compositions, while for x > 0.18, about 10% 3-fold Ge defects are found. The structural properties of these models are compared with the experiment by calculating the total reduced radial distribution function G(r), defined as $4\pi r\rho[g(r) - 1]$, where $g(r)$ is the pair correlation function ($\rho^{-2} < \sum_{i}\sum_{j\neq i}\delta(\vec{r_i})\delta(\vec{r_j} - \vec{r}) >$) and ρ is the density [64]. Fig. 2.1 compares the G(r) calculated from the models with the experiment. Though the peaks of second shells track the experiment, the widths are not perfectly reproduced. Over all, it shows a reasonable agreement between the models and the experiment.

2.2   Topological trends with Composition

The tetravalent (4-fold) Ge and divalent (2-fold) Se are the fundamental building blocks of the Ge-Se network. Starting from x=0, polymeric chain like topology,
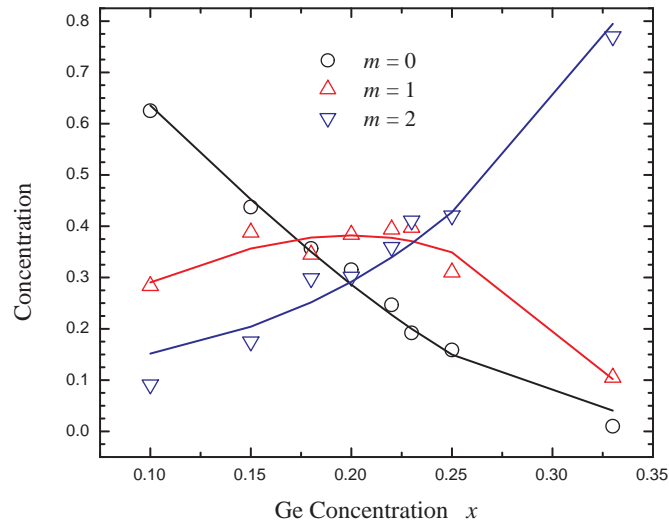
Figure 2.2: Variation of the concentration (%) of 2-fold Se with neighbors m = 0, 1 and 2 fitted with the corresponding probability functions (continuous lines) $a_m + b_m p_m$ (see the text for details).

the system evolves into a network of Ge tetrahedra connected through Se as the Ge content is increased to x=0.33. With increasing Ge concentration, the system gradually eliminates homopolar Se bonds and forms chemically preferred SeGe bonds. A consequence is the transition which occurs in the concentration of three types of 2-fold Se neighbors $Ge_m Se_{2-m}$, where m=0 (Se bonded with 2 Se), 1 (Se bonded with 1 Ge and 1 Se) and 2 (Se bonded with 2 Ge atoms). Fig.2.2 shows the variation of the concentration of three types of structural units Ge_m-Se-Se_{2-m}. At lower Ge content, 2-fold Se have more Se neighbors than Ge neighbors. Increase in Ge content starts to replace Se with Ge atoms as the neighbors of 2-fold Se. At x = 0.20, the concentration of m=1 units assumes a higher value compared to that for m=0 and m=2 units. For

Table 2.1: Fitting parameters a_m and b_m

	a_m	b_m
$m = 0$	0.04	0.98
$m = 1$	0.08	0.60
$m = 2$	0.12	0.70

x>0.23, m=2 units dominate. Following the SICA approach [42], we calculated the probabilities of these units. The three units can be constructed by joining the Se-Se-Se and GeSe4/2 (Ge bonded with 4 Se) molecules, with corresponding probabilities 1-p and $p = 2x/(1-x)$ [42]. The probabilities for m=0,1,2 can now be written as $p_1 = (1-p)^2$, $p_2 = 2p(1-p)$ and $p_3 = p^2$ respectively [42]. Since the models also contains some undercoordinated and overcoordinated atoms, the actual probabilities for these units are written as the linear functions $a_m + b_m p_m$. Parameters a_m represent the possibilities of formation of these units due to undercoordinated and overcoordinated Se and Ge atoms, and b_m are the Boltzmann factors involved in the formation of these structures as described by Micoulaut et al [42]. The coefficient b_m can be interpreted as a measure of the stochastic nature of the formation of unit m with limiting value 1 representing a complete random formation and 0 representing non-random formation. The concentration variation of the three units with composition x are fitted with the these probability functions (Fig. 2.2). The fitting shows a nice agreement between the SICA approach and our models. The fitting parameters are given in the Table 2.1.
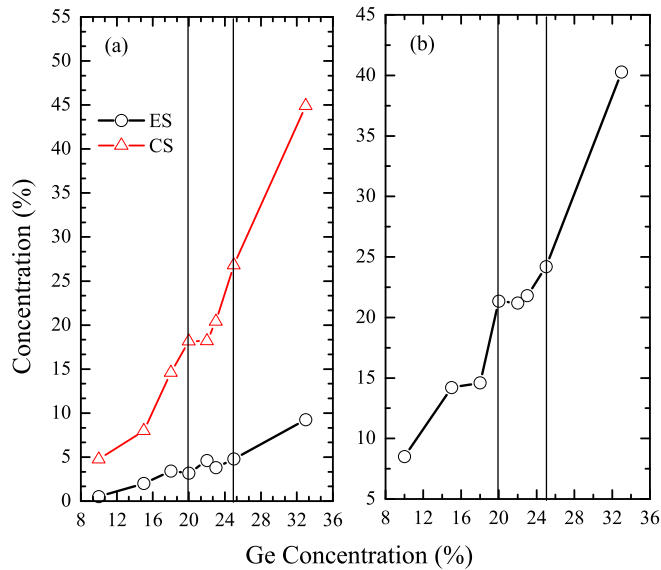
Figure 2.3: Variation of in the concentration of CS, ES and rings (rings up to the size of 10 are counted) with the Ge content. Vertical lines represent the IP range.

The lower value of b_1 shows the decrease in the randomness of the network connectivity in the range x=0.2-0.23, where m = 1 units approaches the higher concentration. Such deviation from the stochastic nature of the connectivity of the network in the IP range (x=0.20 - 0.25) is also revealed in the ^{129}I Mössbauer spectroscopy (MS) experiments. Studies by Bresser et al.[65][66] show that the ratio I_B/I_A of MS integrated intensity due to chemically disorder sites B and ordered sites A deviates from the prediction of the chemically ordered continuous random network (CRN) model.

To see the effects due to the deviation from a complete random behavior, we looked at the variation of structural parameters like corner-shared CS and edge-shared ES tetrahedra and the number of rings presents in the network (Fig. 2.3). A

hint of saturation in the range x∈(0.20,0.23), coinciding with the IP range, for CS and ring concentration is apparent. This is due to the tendency of the network to keep high concentration of $m=1$ units in this range, which poses 'resistance' against the evolution of the network. The saturation of the structural parameters through the IP range thus can be considered as a consequence of the tendency of the network to 'self organise' by preferentially keeping the $m=1$ units in the network.

The non-stochastic nature of the IP is the key to understand experimentally observed anomalies in the structural evolution of these glasses. The extent to what our models show non-random behavior is of course limited by the short time scales involved in the MD simulations. Such non-random behavior present in our models gives some insight, at least qualitatively, into the structural and electronic signatures of the IP at the atomic level.

2.3   Atomistic Picture of the IP

In this section we develop a topological understanding of the IP at the atomistic level extracted from the IP models.

2.3.1   Competing Phases Hypothesis

In order to understand the topological evolution between the compositions x=0 and x=0.33, we start with the hypothesis that the compositions between the a-Se and
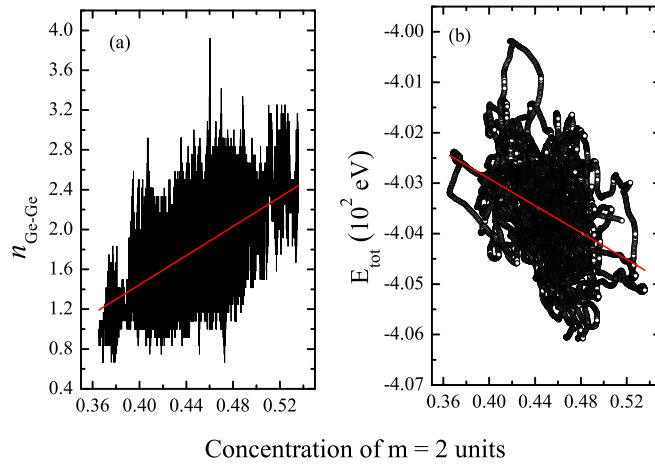
Figure 2.4: (a) The quantity n_{Ge-Ge} is plotted against the fraction of m=1 (Ge-Se-Ge) units. (b) Variation of the cohesive energy of the system with the increase in m=2 units. Straight lines are the linear fit to the data. All the quantities are extracted from 75 ps long trajectory of liquid phase of $GeSe_3$ composition equilibrated at 1200K.

$GeSe_2$ consist of a mixture of the two stoichiometric phases ($Ge_xSe_{1-x} \equiv [GeSe_2]_y +$ $[a\text{-}Se]_{1-y}$)and the intermediate phase appears due to the competition between the two phases, before one of the phase percolates over the whole system. The clustering of Ge Tetrahedra, which can be considered as sub-critical segments of the $GeSe_2$ phase, is also supported by the temperature dependence of A_1 tetrahedral breathing Raman mode, which shows a sudden increase in the liquid phases suggesting the nucleation of Ge tetrahedra [67].

To study the formation of clusters of Ge tetrahedra, we analyzed a 75 ps long trajectory of x=0.25 composition at 1200K. The $m=2$ units can be consider as the unit block of $GeSe_2$ phase, so we quantify the $GeSe_2$ phase (Region A) by calculating the concentration of these units in the system. The clustering of Ge tetrahedra can

roughly be quantified by the average number of second neighbor Ge sites to each Ge atoms (n_{Ge-Ge}) in Region A. For the pure GeSe$_2$ phase, the quantity n_{Ge-Ge} assume the value of about 4.0 depending upon the concentration of edge-shared tetrahedra. Fig. 2.4a shows the correlation between the fraction of m=1 units and n_{Ge-Ge}. Clearly, higher fraction of these units tend to induce clustering of Ge tetrahedra. Such nucleation process is energetically favorable (Fig. 2.4b). The cohesive energy of the system tends to decrease with the increase in the fraction of m=2 units. This suggests that the liquid phase of these compositions contains sub-critical volumes of GeSe$_2$ phase which can give rise to the phase separation at the glass transition temperature. The liquid-gel transition due to the energetically favorable local structures present in the liquid is recently demonstrated [68].

2.3.2 Evolution of the Two Phases

To understand the network evolution with composition, we divide the cells into three regions. Region A, as defined above, consists of clusters of Ge-Se tetrahedra (CS/ES tetrahedral units), region B consists of short Se$_n$ chains, where $n = 2 - 5$ is the number of Se in the chain, joining the Ge sites and the region C consisting of the rest of Se background which represent the a-Se phase. Fig. 2.5 shows the variation of Ge and Se sites in the three regions. Rapid increase of the Ge content in region A (Fig. 2.5a) shows the tendency of Ge tetrahedra to form clusters rather than dispersing uniformly in the network. The Ge content in region A shows saturation in
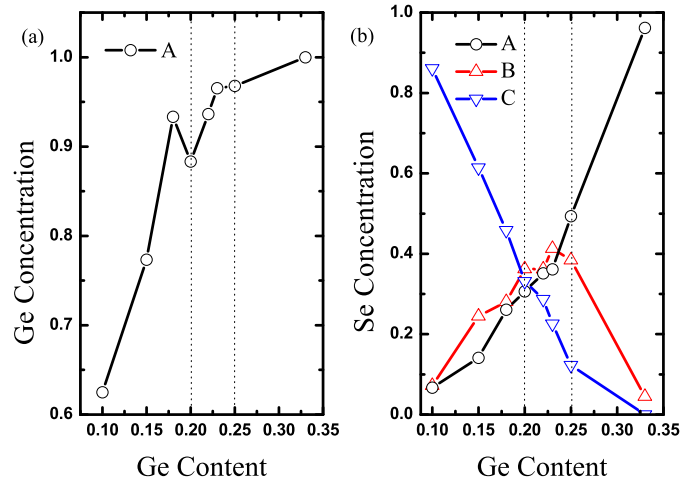
Figure 2.5: (a) Variation of concentration of Ge sites in region A. (b) The variation of Se sites in the three regions. Region A: GeSe$_2$ fragments; B: short Se chains; C: long Se chains (see text). The dotted lines represent the IP range.
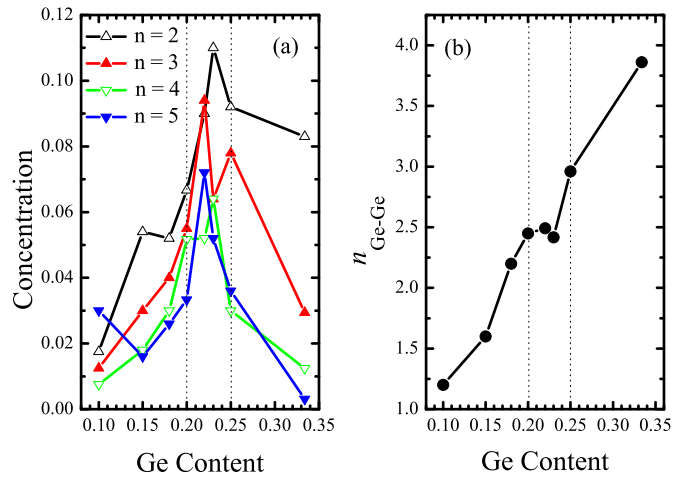
Figure 2.6: a) The concentration of short Se$_n$ (n=2,3,4,5) chains plotted against Ge content. b) Variation of n_{Ge-Ge} (see the text) with Ge content. The apparent saturation between $x = 0.20$ and 0.23 reflects the 'delay' in the growth of the clusters of Ge tetrahedra.

the IP range after rapid increase in the Se rich compositions. The saturation suggests that the clustering of Ge tetrahedra doesn't increase monotonically through the IP window. The Se sites in region B (short Se chains) reach a maximum concentration inside the IP window (Fig. 2.5b). The concentration of short Se_n chains is shown in Fig. 2.6a. The Se short-chain concentration assumes its maximum in the IP window. This is consistent with the variation of Se chain (CM) Raman mode, which splits into lower and higher frequencies (ascribed to the short Se chains) above $x = 0.19$ as observed in the Raman measurements on Si_xSe_{1-x} [69] glasses, whose topology is believed to be fairly similar to that of Ge_xSe_{1-x} glasses. The variation of Se sites in the three regions suggests that in the IP window most of the background a-Se phase is consumed by region A and B. Above the IP range the concentration of Se sites in region A increases at the cost of region B.

The compositions in the IP range are characterized by clusters of Ge tetrahedra and short Se_n chains. To understand the growth of region A with the increase in the Ge content, we plot n_{Ge-Ge} versus the Ge content (Fig. 2.6b). The increase in n_{Ge-Ge} indicates the expansion of region A. As suggested by Fig. 2.6b, n_{Ge-Ge} saturates in the IP window. This shows that in the IP range, the system tends to resist the percolation of $GeSe_2$ phase, which causes the apparent 'flattening' in the evolution of structural parameters like CS/ES tetrahedra (Fig. 2.3). Such a behavior suggests self-organization (SO) in the connectivity of the network as suggested by others [41]. The evolution of the topology of region A and B is shown in Fig. 2.7. Note the
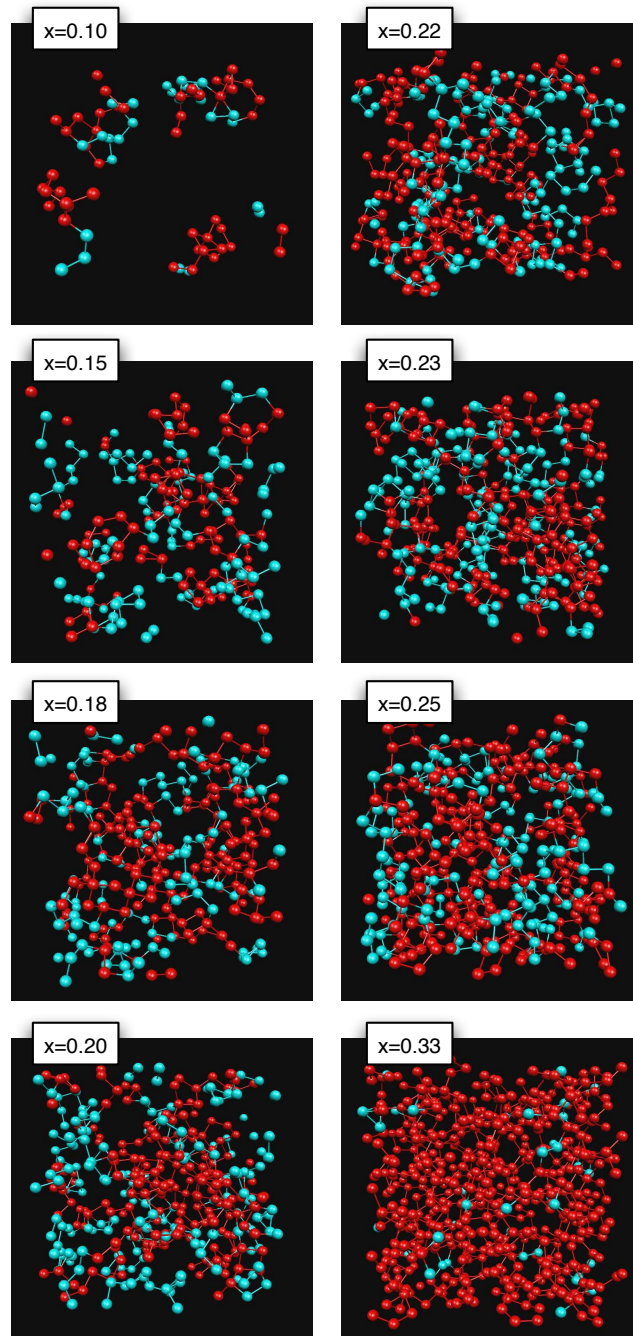
Figure 2.7: Two-dimensional projection of the spatial distribution of "region A" (GeSe$_2$ CS/ES tetrahedra) and B (short Se chains) is shown for different compositions. Red and blue sites represent atoms in region A and B respectively. The role of short Se chains as a barrier between GeSe$_2$ clusters is seen for compositions in the IP window. The black background is polymeric Se. Note the clustering (non-randomness) of the GeSe tetrahedra, even for low Ge concentration.
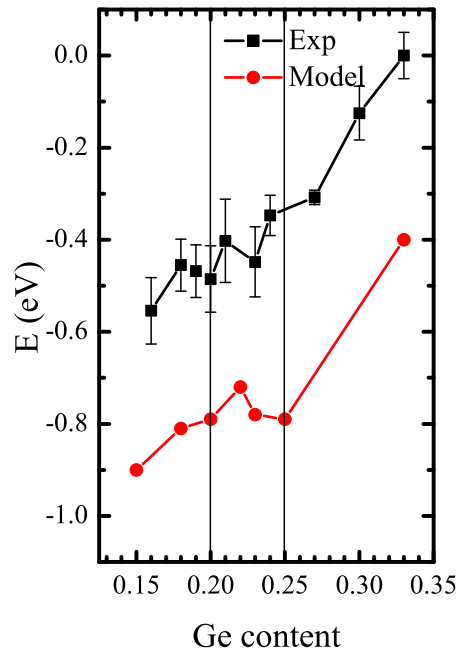
Figure 2.8: the shift in the average conduction edge energy $\langle E_c \rangle$ with compositions 'x'. The absolute values are shifted with a constant for comparison with the shift in the WL positions (relative to the composition x=0.33) for Se atoms in the K-edge XANES spectra (details of the experiment can be found in [72]).

obviously non-random nature of the positions of the GeSe tetrahedra, especially the

clear tendency for the tetrahedra to cluster, even for small x. The short Se chains

appear at the boundaries of $GeSe_2$ clusters. In the IP window, between 0.20 and 0.23,

the density of region A seems to saturate, as suggested by Fig. 2.6b until it covers

the whole cell at $x = 0.33$.

2.4 Electronic Signature of the IP

The addition of Ge in the a-Se network nucleates clusters of Ge tetrahedra (region A), which can be considered as harbingers of g-GeSe$_2$ since CS/ES tetrahedra are the building blocks of this network. Due to the cross-linking at Ge sites, these clusters are surrounded by short Se$_n$ chains (region B). Increase in cluster size also increases the concentration of Se$_n$ chains at the cost of the background a-Se (region C). Region B acts as a 'barrier' against the formation of GeSe$_2$ (volumes of type A), thus resisting the percolation of region A. The IP appears when most of the a-Se background "C" is transformed into short chains "B". The system has many subcritical fragments of g-GeSe$_2$ phases and the remainder is short Se$_n$ chains. Appearance of such a mixed phase is the cause of the apparent delay in the evolution of the network [63], characterized in various experiments as a flattening of observables for x in the IP window. Further increase in the Ge content causes cross-linking in region B, and thus region A percolates all over the system. It suggests that the evolution of region B defines the width and the position of the IP on the composition scale. As Ge atoms tend to form clusters rather than getting dispersed, it ensures the persistence of region B in the IP window. In this picture the existence of the IP is due to the appearance of short Se chains. Severing these chains would result in the collapse of the IP. This may explain the reduction in the width of the IP due to the addition of Iodine for the $x = 0.25$ composition [70].
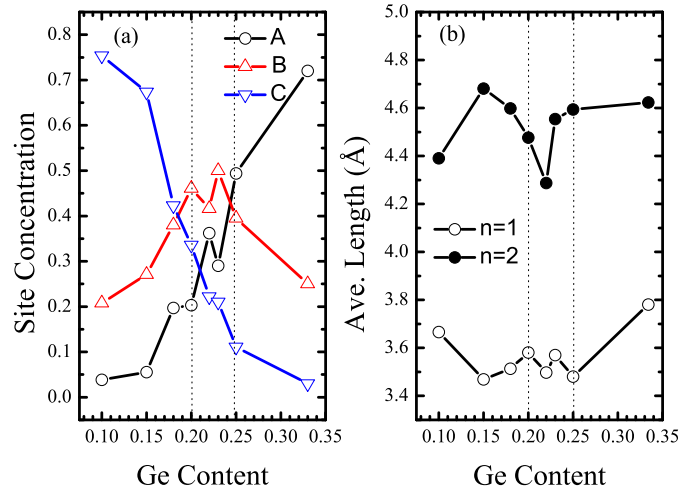
Figure 2.9: a) Concentration of sites representing the three regions (A, Ge-Se tetrahedra; B, short Se chains; C, long Se chains, see text), which contribute to ten localized states at the valence and conduction tails for different compositions (see text). b) Variation of the average lengths of $n = 1$ and $n = 2$ chains with the Ge content. Vertical dotted lines indicate the experimental width of the IP.

Earlier PES and IPES studies [30] on Ge_xSe_{1-x} glasses reveals a shift in the conduction band tail at x=0.2 in the electronic density of states, while no apparent shift is observed for the Valence band tail. Our models also show the shift in the tail states above fermi level into the band gap in the IP window, with no considerable shift in the valence tail states.. Looking for the possible electronic signature of the IP, we obtained the shift in the conduction band edge (Fig.2.8) by calculating the average conduction edge energy $\langle E_c \rangle = \int_{cb} \epsilon \rho(\epsilon) d\epsilon$, where $\rho(\epsilon)$ is the electronic density of states and cb specifies a quadrature range starting at the Lowest Unoccupied Molecular Orbital edge, extending 2.0 eV into the conduction band[71]. The shift is compared with the shift in the white line (WL) position for the Se atoms in the K-edge XANES

spectra which represent the shift in the conduction band. The agreement between the models and the experiment is pleasing. both show a "plateau" close to the indicated IP window, both show similar positive slope to the right and left of the IP window. Overall, there is a significant resemblance, considering that there are no free parameters, and now we have an electronic experiment that shows "IP flattening", as seen by Boolchand and others [26] for other observables.

To get further insight into the electronic properties, we look at the evolution of the atomic sites, belonging to three topological regions defined above, which contribute to the conduction and valence tail states. Fig. 2.9a shows the concentration of atomic sites in regions A, B and C contributing to the localization of the tail states (atomic sites contributing to the localized states are identified by projecting the eigen states on the atomic positions). In the IP range, tail states are mostly localized in region B, which is understandable as this region appears around clusters of tetrahedra due to cross-linking and thus becomes strained as the size of the clusters and the content of this region increases to a maximum in the IP window.. Since in the IP range, the band tails states are mainly residing on these short Se chains, the IP would also be sensitive to the light illuminations as the micro Raman studies suggests [73]. The strain on short $n=1$ and $n=2$ chains, in the IP window is clear in fig. 2.9b, which shows the variation in the average lengths of these chains with the Ge content. In the IP window, $n=2$ chains shows a clear decrease (bending) in the IP window and the average length of $n=1$ shows a 'plateau' like behavior in the IP range. In order to

see the effect of the bending of these chains on the electronic spectrum, we studied a toy model consisting of these two chains attached to each other. The decrease in the lengths of these chains show a clear downward shift in the eigenvalues above the fermi level compared to the relaxed system, which suggests that the antibonding states of this system are more sensitive to the bond angles residing on Se atoms.

CHAPTER 3

Silver-traps in a Solid Electrolyte $(\text{GeSe}_3)_{0.85}\text{Ag}_{0.15}$

work is published in I. Chaudhuri, F. Inam and D. A. Drabold, Phys. Rev. B 79 100201(R) (2009).

Silver-doped Ge-Se glasses exhibit a fascinating range of phenomena: among them are high ionic conductivity[50] and photo-doping[75], connected with high Ag diffusion[53][51]. An empirical model of Elliott [76] provides an estimate of the activation energies of ionic conductivities. In this model the Ag ions are assumed to be surrounded by cations (Se), and Coulombic and polarization interactions give rise to the potential barriers, leading to the hopping dynamics of Ag. The first MD simulations, using an empirical potential, are due to Iyetomi *et. al*[77], who detected phase separation of the Ag atoms in GeSeAg glasses. Recently, the existence of Scher-Lax-Phillips traps[78] is reported, in *ab initio* models of $(\text{GeSe}_3)_{1-x}Ag_x$ (for $x = 0.10$ and $x = 0.15$)[58]. Our calculations are related to a recently-published percolative free-volume model[79], and provide microscopic identification of the trapping centers proposed by these and other authors.

In fast-ion glass conductors, one of the basic problem is the understanding of the ion hopping in the disordered network. In this chapter, as a step toward a general

atomistic picture, we present a detailed *ab initio* study of Ag dynamics in a glassy germanium selenide matrix. In agreement with a previous study[58], we show that trapping centers exist, and for the first time describe their atomistic nature in detail. Our work is also related to the theory of batteries, the prime technological application of solid electrolytes. Finally, the promising "Programmable Metallization Cell", a novel non-volatile computer memory device [74][56] is made from the materials we describe here.

The dynamics of Ag at different temperatures is thoroughly discussed. We find that Ag atoms sit preferentially near the midpoint between the host (Ge or Se) atoms separated by about 5.2Å at T=0, and we name these energy minima as "Trapping Centers" or TC. For $T > 300K$, there is hopping between the TCs, but this is spatially non-uniform, and even temperature dependent. We find that the TCs are non-uniformly distributed in space, mostly present in Se rich region of the glass network. Volumes with a high concentration of TCs have longer trap lifetimes than volumes with few or no TCs. The barriers between TCs that are close together tend to be small, enabling rapid hopping *within the high density region*, but the effect of a collection of TCs in close proximity is to create a strong barrier for the Ag to escape to another volume. Thus, one can introduce the notion of "supertraps" or cages, associated with a high concentration of TCs. Ag dynamics at finite temperature can be understood to be cage-cage hopping with larger trapping time at low temperatures.
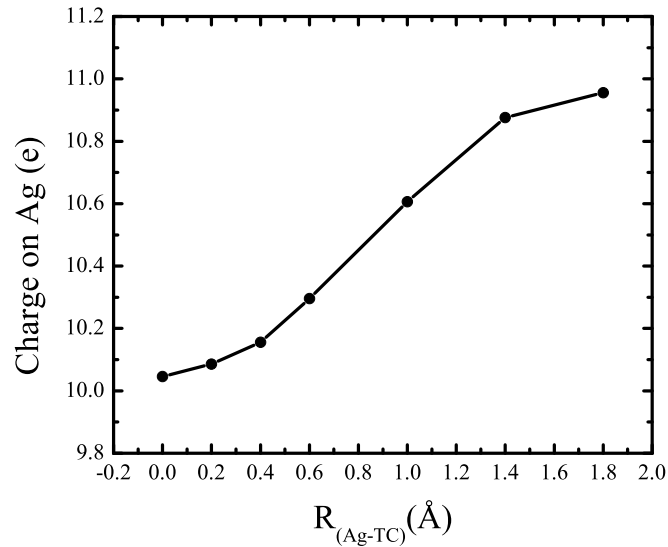
Figure 3.1: Valence charge on Ag site with respect to the distance from the TC site (see text). The charge state of Ag changes from neutral when isolated to ionic near TC. Neutral silver has 10 3d and one 4s electrons.

Our simulations provide dynamics reminiscent of motion in supercooled colloids[80] and diffusion of Li ions in silicate glass[81, 82, 83].

3.1 Solid Electrolyte Model

The results reported here are from the plane-wave **ab initio** code VASP[61] (Vienna *ab initio* simulation package) at constant volume. We began with a 239 atom $(GeSe_3)_{0.85}Ag_{0.15}$ model (50 Ge, 153 Se and 36 Ag atoms), generated with the local basis *ab initio* FIREBALL method[84], with a neutron structure factor close to experiment. We relaxed this model with VASP by minimizing the total energy of the

cell. Only small changes were noted after relaxation. Details of coordination and structure are reported in [58] In the model, the nearest neighbor structure around Ag show an interesting feature that all Ag atoms are positioned halfway between pairs of host atoms (Ge-Ag-Ge, Se-Ag-Se or Ge-Ag-Se), with the exception of only one Ag. About 61% of Ag sites reside between pairs of Se atoms, the rest involve one Ge. The distances between host pair atoms is between 4.7 to 5.2 Å and the bond length of the Ag to the atoms of the pair is in the range 2.4 - 2.6 Å. About 17% of Ag have 2-fold Se neighboring pair, the rest of the Ag host pairs are under-coordinated. To verify the existence of these traps in an independent way, we introduced un-bonded Ag atoms at different locations in a 96-atom amorphous $GeSe_3$ model at T=500K, so that the Ag could "probe" the energy landscape in an unbiased fashion and without exception, all the Ag became trapped between pairs of host atoms with distances in the range indicated above.

First we look at some electronic characteristics of the Ag in the solid state. We examined the charge state of Ag by removing all but one Ag. It is found that the remaining Ag lost a charge of about one electron when moved from an isolated position to a TC. Near a TC, Ag acts as a positive ion [75]. At TC, about 65-70 % of the charge lost by Ag site is transferred to the neighboring pair sites. Thus, in the Born-Oppenheimer approximation (expected to be valid here), we find Ag to be uncharged while undergoing diffusive motion, and in the Ag^{+1} state for bonded conformations (see Fig. 3.1). This suggests that the metallic Ag filaments of the PMC are only

weakly bonded to the network, while the Ag atoms in the filament are chemically bonded to each other.

Silver in the $GeSe_3$ network is found to affect the electronic density of states near the optical gap. In 239 atom model a considerable contribution from the Ag neighbors to the valence edge states is observed. To get further insight, we introduce one Ag in 96 atom $GeSe_3$ model at an isolated position (at a distance of 3.0 Å from the glass network) and few Ag at the TC sites. For non-bonded Ag, it is found that a silver-related level appears about 0.2 eV below the LUMO level. An increase in the contribution to the valence edge levels due to the Ag neighbors, for Ag at TC sites, along with the increase in the charge on these sites is observed. A slight increase in the Ag contribution to the conduction edge levels is also noted. Further, to see the effects due to the change in the occupancy of the band edge levels, we added an extra electron to the system to occupy the LUMO (lowest un-occupied molecular orbital). It is found that the total charge on Ag sites is increased and consequently the contribution of Ag to the conduction tail is enhanced. The increase of charge on Ag sites resulted in an increase (7-10%) of bond length between Ag and the neighboring pair sites. These observations are important in understanding the optically enhanced diffusion of Ag in the glass. Light of an appropriate wavelength might induce electronic transitions between the valence tail and conduction tail states, both of which are Ag-related as suggested by these observations. Hellmann-Feynman forces associated with light-induced occupation change may be large for the Ag, and

can stimulate metal diffusion in a local-heating picture[85]. Also, addition of an electron (mimicking light-induced occupation change) suggests weakened Ag bonding, thus lower barriers, and consequently more diffusive Ag.

3.2 Dynamics

Silver dynamics is studied by constant-temperature Nosé-Hoover dynamics at 300K and 700K. Extended trajectories of 20ps were obtained. The mean squared displacement (MSD) of all the atomic species is calculated as $(1/N)\sum_{i}(r_i(t) - r_i(t_o))^2$, where $r_i(t_o)$ and $r_i(t)$ are the positions of atomic site 'i' at initial t_o and later time t respectively. The MSD for Ge, Se, and Ag at different temperatures is shown in Fig.3.2. The Ag atoms at 700K show large MSD compared to that at 300K, consistent with the previous studies [58]. At 300K, the Ag dynamics is qualitatively different compared to that at 700K. At 700K, the MSD of Ag increases almost linearly suggesting a diffusive dynamics, while at 300K, it saturates quickly to a level higher than that of covalent (Ge,Se) network. This suggest a 'trapped' diffusion at low temperatures. The average diffusion length (average displacement from the initial position) for Ag for the 20 ps duration is found to be about 1.0 Å at 300K, while at 700K it varies up to 6.0 Å. Presence of Ag at the TC also effects the dynamics of the neighboring TC sites. To compare the dynamics of pairs of host sites with and without Ag at their centers, we calculate the root mean squared fluctuations $\sigma(R)$ ($\sqrt{< (R(t) - R_{eq})^2 >}$), where '$R(t)$' is distance at an instant 't' and 'R_{eq}' is the mean distance in equilib-
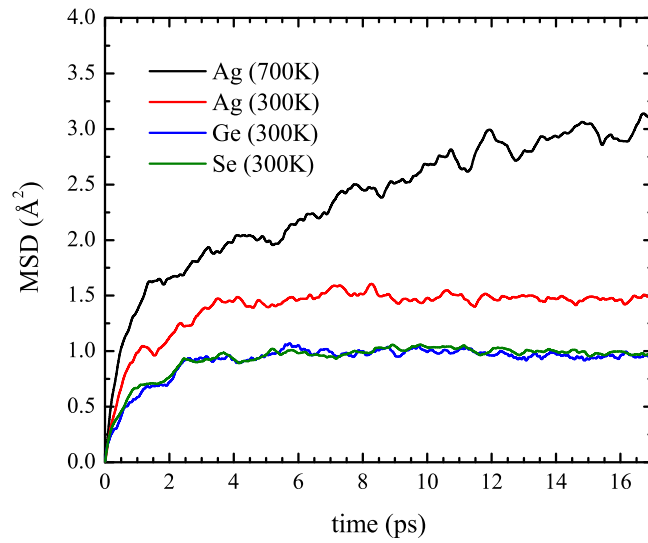
Figure 3.2: Mean squared displacement of Ag, Ge and Se is shown at 300K and 700K.
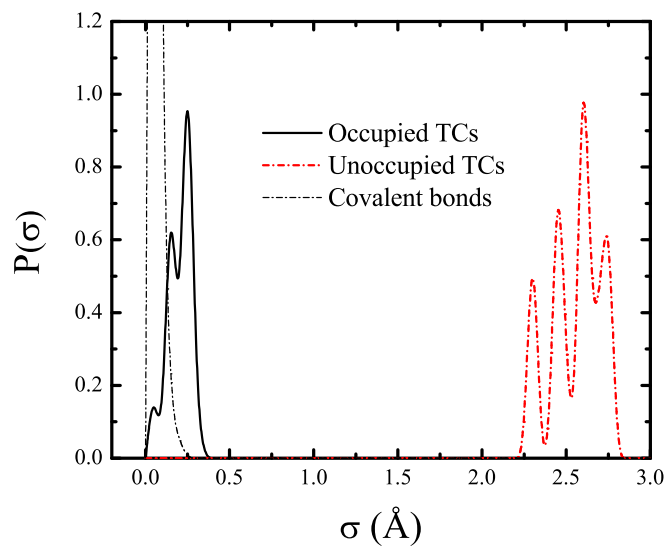
Figure 3.3: The distribution of the root mean fluctuations 'σ' at 300K is shown for the TCs pair distances, when they are occupied by the Ag and when they are unoccupied. Distribution of the root mean fluctuations in the Ge-Se and Se-Se bond lengths are shown for comparison.

rium) about the equilibrium TC pair distances. Fig. 3.3 shows the distribution of
'$\sigma(R)$' for occupied and un-occupied TCs along with that of Ge-Se and Se-Se bond
lengths at 300K. Clearly, the presence of Ag sharply reduces the fluctuations in the
pair distances closer to that due to the covalent bonds. This suggest a vibrational
signature of the presence of Ag at TCs.

3.2.1   Ag Hoping at 300K

At 300K, silver is largely trapped: only 6 hopping events were observed. The silver
traps fall into two categories. *Type 1* (32%) are strongly bound: 4 Ag atoms sit at
single TC with no neighboring TC within a radius of 2.0 Å, and 7 Ag occupy two
overlapping TCs with the host pairs making an angle of about 90° to each other. *Type
2* (68%) are oscillating between two or three closely spaced TCs. Fig. 3.4 elaborates
the dynamics of the two types of Ag. In the top panel of Fig. 3.4, dynamics of Ag_{213}
(type 1) relative to the three TCs is shown. Initially it is trapped at TC(11-202)
(between Ge_{11} and Se_{202}), the gradual decrease in the Ge_{11}-Se_{202} distance pushes the
Ag out and it is eventually trapped at two overlapping TCs [TC(60-202) and TC(11-
98)]. Note the stabilization in the Se_{60}-Se_{202} and Ge_{11}-Se_{98} distances after Ag is
trapped between the host atom-pair. The bottom panel of Fig. 3.4 illustrates type 2
Ag silver motion. Ag_{228} is initially trapped at TC(107-142). It becomes unstable due
to the motion of TC(142-150), (initially at 1.8 Å from Ag_{228}), and then a decrease
in the Se_{107}-Se_{142} distance moves it out of its initial TC. Eventually Ag_{228} is trapped
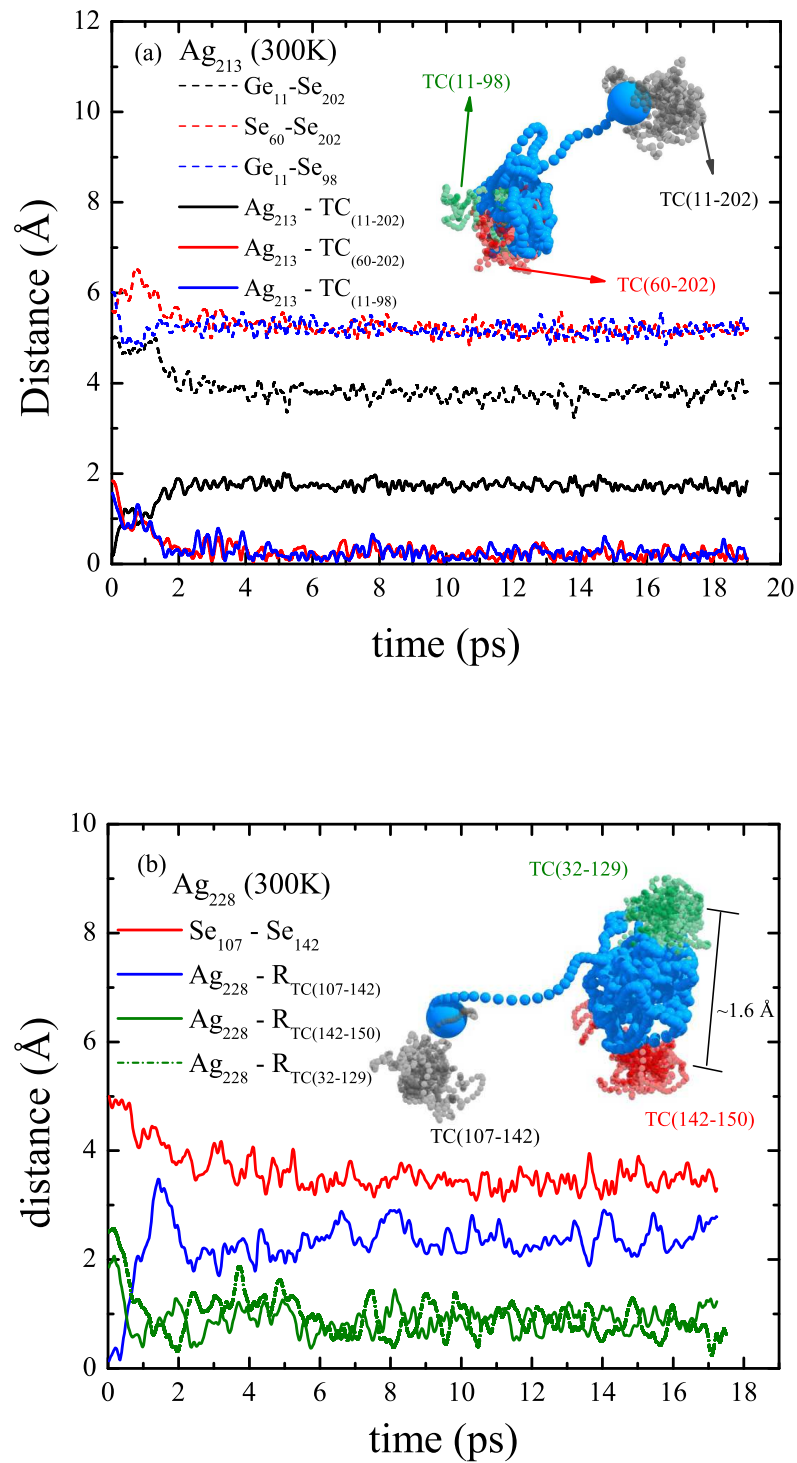
Figure 3.4: Characteristic examples of silver dynamics: Top: "Type 1" trap, Bottom "Type 2" (see text). The inset shows the trajectories of Ag sites (blue) with the trajectories of neighboring TCs (grey, green and red).

between the two TCs [TC(142-150) and TC(32-129)] with an average distance of about 1.6Å between them. The trajectory of Ag_{228} shows cage or "super-trapping" between two TCs. Note the larger fluctuations in the position of Ag as compared to type 1 Ag (trajectory of Ag_{213}). The hopping lengths between one TC to other TCs, in general depend upon the concentration of neighboring TCs. A larger number of neighboring TCs tends to confine the Ag in a smaller region (1.0 Å) as in the two cases discussed above, while larger jumps are observed for Ag with lower concentration of neighboring TCs.

3.2.2   Ag Hoping at 700K

The mean squared displacement of Ag at 700 K shows a linear increase with time, illustrating the diffusive nature of the Ag dynamics, consistent with the previous studies [58]. The Ag dynamics consists of a gradual drift away from the initial (fully relaxed) TC configurations, followed by hops between cages. There are 20 jumps observed, much larger than that for 300K, as expected, with an average time period of *ca.* 7 ps between the hops. The hopping lengths vary between 1.5 - 4.0 Å. We characterize such hopping dynamics in terms of the variation in the concentration of TCs n_{TC} around Ag sites. Fig. 3.5 shows the displacement of Ag_{213} at 700K. The hopping is apparent in the form of abrupt changes in the displacement. To understand these jumps, we counted the number of TCs surrounding the Ag site in a radius of 4.0 Å. In Fig. 3.5, the concentration of neighboring TCs is also plotted

with the displacement. A correlation between the hops and the decrease in n_{TC} is apparent. The jumps tend to occur at times when either n_{TC} is low or exhibits a sudden decrease. Also, the figure reveals the significant impact of thermal fluctuations on the TCs and their density. The trajectory of Ag_{213} along with the trajectories of three neighboring TCs (inset) in the trapped region gives further insight into the nature of the trap. At higher temperature, the Ag sites are more unstable because of thermal fluctuations in the neighboring network and their higher thermal energies. It would require a higher density of TCs to confine the Ag dynamics. The hops can be considered as a spontaneous event, which may be triggered by a decrease in the concentration of neighboring TCs.

3.2.3 General Picture

Fig.3.6 illustrates Ag motion at both temperatures. In equilibrium, the Ag at 300K are confined on or in between the dense regions spanned by the TCs. Note that the volume fraction containing no TC is large at 300K. At 700K, TCs are less concentrated owing to the thermal fluctuations in the host network, thus enhancing Ag diffusion. The Ag jumps between dense TCs regions (cages) is apparent. Such dynamics is quite similar to the hopping dynamics suggested for Li ions in silicate glasses [82, 81], where the high mobility of Li ions is correlated with the decrease in the volume fraction of voids, which decreases the local atomic density around ion [83, 80]. At 300K, the TCs are relatively more stable and are distributed randomly
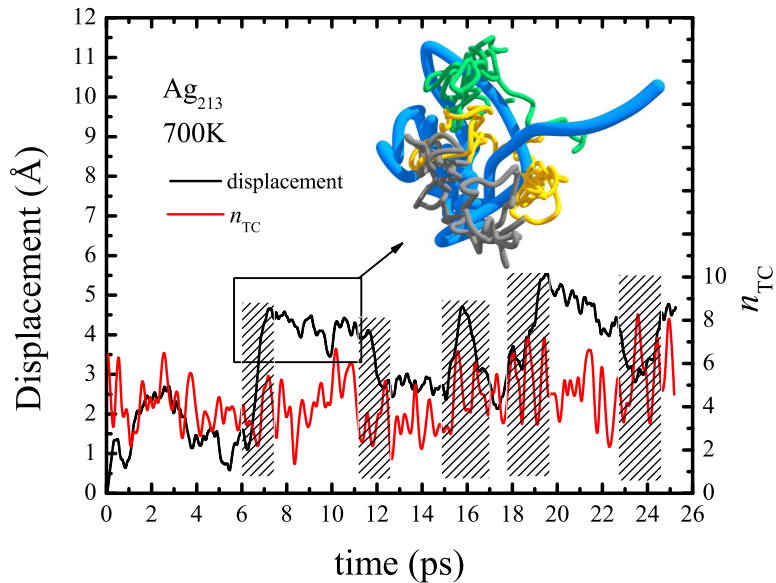
Figure 3.5: Displacement of Ag_{213} and the average number n_{TC} of trapping centers surrounding Ag_{213} (within the radius of 4.0 Å around the Ag atom). The shaded regions highlight the hops. The trajectory of Ag_{213} (blue) is shown along with those of three neighboring TCs (yellow, green and grey) in the time during which Ag is trapped after making a 'jump'.

as shown in Fig. 3.6 in the form of dense and dilute regions, similar to the Scher-Lax-phillips traps [78]. One can view Fig. 3.6 as revealing a percolation-like process: at the higher temperature the trapping basins become more extended and overlapping, until transport through the glass becomes possible.

3.3   Ag Coordination State

At the end we make some qualitative remarks regarding the Ag coordination state in the glass network. The topology of the TCs and the higher diffusion of
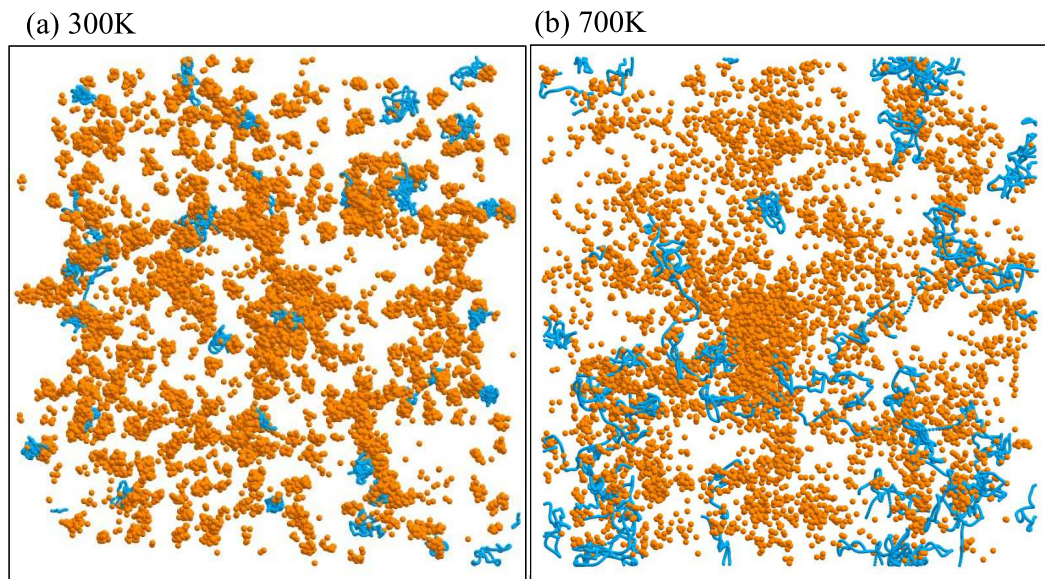
(a) 300K

(b) 700K

Figure 3.6: Trajectories of TCs (orange) and all Ag (blue) in equilibrium (of about 6 ps length) are shown at (a) 300 K and (b) 700K. Concentration of Ag sites around dense regions of TCs is apparent at 300K and the Ag hops between the dense regions of TCs are clear at 700K.

Ag suggest a weaker and lesser covalent nature of the Ag bonding. The number of nearest neighbors of Ag thus depends upon the local atomic configuration around Ag which can present single (which gives Ag coordination 2) or overlapped multiple TCs (coordination 3 or more) for Ag. The Ag coordination in this picture would also depend upon the Ag concentration and the topology of the with host network. The coordination would increase with the Ag content as the possible ioslated TC sites, which can accommodate Ag, saturates and the Ag accumulation on overlapped TC sites increases. The coordination state also depends upon the topology of the host network. In Se rich compositions with relatively *open* network, Ag can easily

be trapped at single TCs, while more *compact* rigid compositions closer to x = 0.33 would only provide overlapped TC sites and thus the Ag coordination would tend to increase with the Ge content also. The Ag incorporation in the glassy network thus would depend considerably on the host network. The higher glass forming ability of Ag added Ge-Se compositions in the IP window is already reported [49].

CHAPTER 4

Theoretical Study of amorphous GeSe$_2$ surface.

The binary chalcogenide glass g-GeSe$_2$ has been extensively studied for its structural and optical properties. The microscopic nature of atomic order beyond the nearest neighbor distances has long been a controversial subject. There are two main approaches to address the structure. One is the chemically ordered covalent random network approach, first developed by Zachariasen [3] and later used by Tronc *et al.*[86] to interpret their optical-absorption edge and Raman-scattering results on Ge$_x$Se$_{1-x}$ alloys. In this model chemically wrong bonds are forbidden. Another approach is by Bridenbaugh *et al.*[87]. It explains ordering as arising from a quasi-ordered structural unit, presumably reminiscent of a crystalline phase, in which wrong bonds exist as an integral part. The presence of chemical disorder has been experimentally confirmed by Boolchand *et al.*[88] and Petri *et al.*[36]. The first principles molecular dynamics model of g-GeSe$_2$ by Cobb *et al.*[8] is also reported a significant fraction of homopolar bonds. Concentration of wrong bonds in these models is found to vary when such models are relaxed at different pressures [89].

Surface properties of disordered materials are relatively less known compared to the crystalline counterpart. Though the experimental surface techniques like STM have been applied to a-C:H [90] and a-Si:H surfaces [91] with some success, it is found difficult to apply such techniques to amorphous surfaces in general due to the lack of periodicity or surface roughness. Theoretical modeling of amorphous solid surfaces can be divided into two categories, models generated with molecular dynamics (MD) simulations based on semiempirical potentials and the first principle methods. Earlier work by Garofalini [92] [93] on amorphous silica surfaces, using classical MD techniques, provides basic understanding of the structural properties of amorphous surfaces. Similar methods were used to study other amorphous oxides like Al_2O_3[94]. In the last decade first principle MD simultion based surface models of a-Si [95], a-Si:H [95],**liquid**-Si, [96], a-C [97][98] and gGeSe$_2$ [99], were reported. In most of these studies, the scheme used to form a surface is same as is used for crystalline surface; minimizing the total energy of the supercell with boundary conditions applied in two directions only, leaving two free unreconstructed surfaces. This scheme, though successful in the study of crystalline surfaces, has a disadvantage. It is able to explore only a limited class of configurations near the truncated bulk. In this chapter, the surface model $GeSe_2$ is presented.

The surface of glassy $GeSe_2$ is generated using quench from melt technique, which is found successful in modeling bulk glasses [8][9]. The glass slab with two free surfaces is obtained by quenching the equilibrated liquid slab. The resulting slab shows the
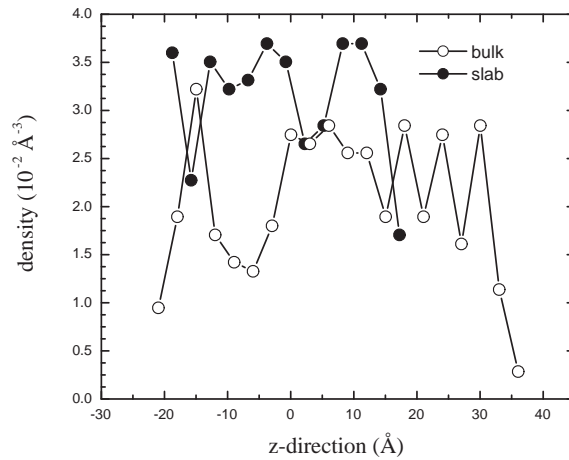
Figure 4.1: Density fluctuations in bulk and slab. Atoms are counted in layers of 3.0 Åwidth along the z-axis.

outer layers reconstructed by the formation of rings of different sizes bundled together. Coordination statistics show improved bonding configurations. Vibrational spectra of the slab reveals the mixing of A_1 and optical band due to a slight increase in the Ge-Se bond length. The width of the slab is found to expand, most probably due to the zero pressure at the two surfaces. In the absence of any experimental characterization of these surfaces, these results are presented as predictions.

4.1 Model Generation

Simulations were carried out using the density functional local basis *ab initio* code 'Fireball' [60]. The approximation used are Harris functional and local density

Upper Layer
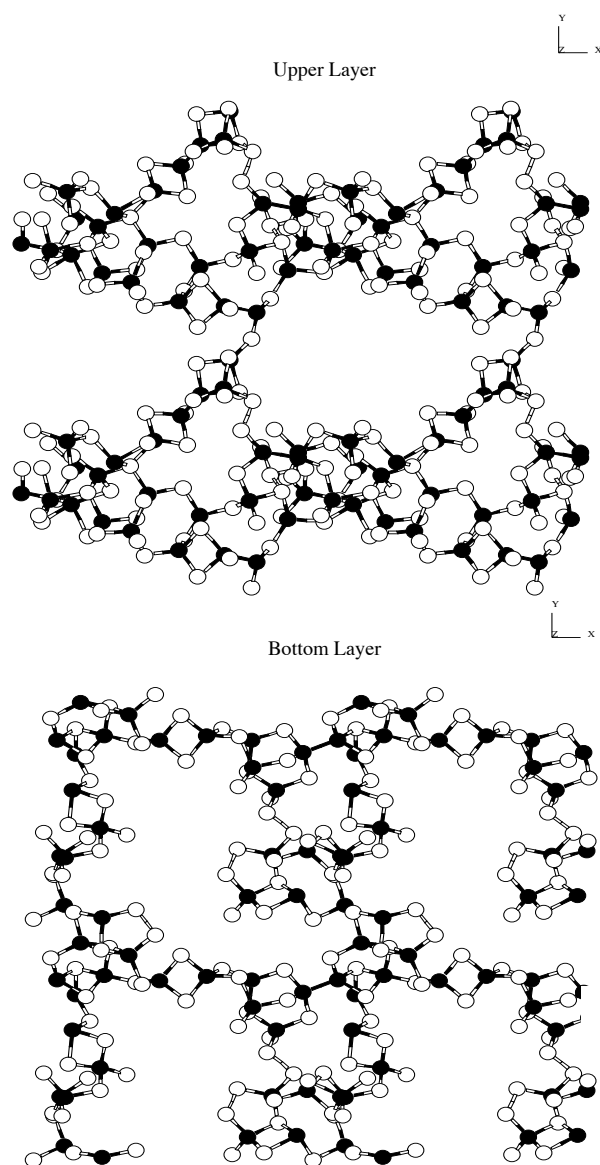
Bottom Layer

Figure 4.2: Upper and bottom surfaces (8 Å thick) of the slab are shown. Filled circles represent Ge atoms and empty circles represent Se. Periodic boundary conditions are used to reveal four copies of the layers in the xy plane to emphasize the ring network.

approximation (LDA) and single ζ basis. For the $GeSe_2$ surface, we started with the 216 atom (18.76 Å) bulk model by Cobb *et al.*[8] which shows reasonable agreement with the experiment. To construct a surface model we joined two copies of the Cobb cell in the z-direction to get a rectangular cell of 432 (144 Ge and 288 Se) atoms. In this way we get a reasonable thickness in the z-direction to see if the middle portion of the cell could preserve the bulk features for the comparison. The system is relaxed in the slab geometry by breaking the periodicity in the z-direction to get a 'relaxed' truncated bulk. It is then melted *in the slab geometry* at 1100K. The liquid phase is obtained by equilibrating the system at this temperature for 8 ps using microcanonical MD with a time step of $2.5fs$. To obtain the amorphous phase, the liquid slab was slowly cooled to room temperature ($300K$) over a period of about 8 ps. After equilibration for 2.5 ps, it was steepest descent quenched to $0K$. The total energy of the resulting slab is found to be $37meV/atom$ lower than that of the relaxed truncated bulk. Annealing at high temperature in the presence of a vacuum between the copies of the cell caused the system to expand from the initial bulk thickness in the z-direction. To control the expansion of the width, An alternate method is applied to generate the surface of $GeSe_3$ (Appendix A), where the truncated bulk is equilibrated at temperature below the melting point. Fig. 4.1 plots the local density in the slab and bulk along z-axis. Upper and bottom layers are shown in Fig. 4.2.

4.2   Coordination and Ring Statistics

First we look at the bonding configurations in GeSe$_2$ slab. Overall, coordinate statistics do not differ significantly between the surface and bulk. Both chemical ordering and the 8-N rule is some what better satisfied on the upper and bottom layers relative to the interior of the slabs. Homopolar Ge-Ge bonds are *decreased* to 1.4% of the total number of possible bonds ($4N/3$, N is the number of atoms in the system) when bonding criteria for Ge and Se is satisfied, as compared to 3.5% Ge-Ge bonds present in the bulk. Similarly Se-Se bonds are decreased to 6% from 8% bonds in the bulk model. This seems consistent with the pressure induced effect on this system as studied by Durandurdu *et al.*[89]. The reason could be that quenching the system in the slab geometry is thermodynamically similar to the quenching under constant pressure. Such improvement in the chemical order has directly affected the ring structure of the system.

Table 4.1 compares the number of different size rings in the GeSe$_2$ slab to that in the bulk. The number of rings has increased relative to bulk, with specific increase in the even size rings as compared to odd size rings, which is the consequence of the decrease in the homopolar bonds. Upper and bottom layers are characterized by the formation of rings of different sizes attached together as shown in Fig.4.2. About 94% of the atoms in these layers constitute the ring network.

Table 4.1: A comparison between n-fold rings in bulk and slab model.

n	3	4	5	6	7	8	9	10
bulk	6	40	20	44	4	18	14	8
slab	0	44	23	47	12	29	12	20
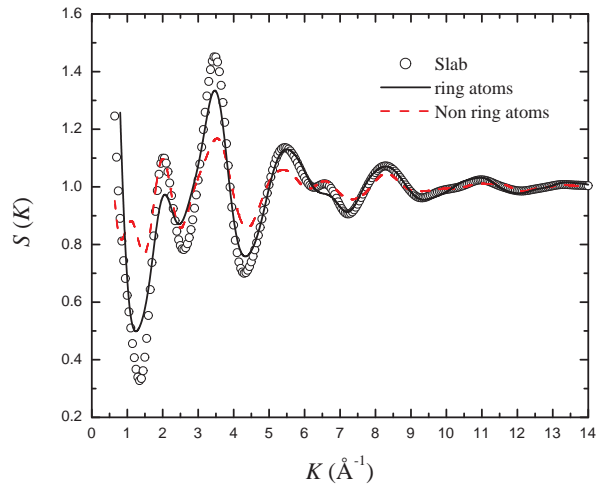
Figure 4.3: $S(K)$ calculated from the atoms which are part of rings of sizes 4 to 10, and from the atoms which are not part of these rings. The two curves are compared to $S(K)$ from the whole slab.

4.3 Structural Properties

Structural properties of the glass slab are studied by calculating the pair correlation functions $g(r)$ and static structure factors $S(K)$. To study the contributions to $S(K)$ from different parts of the slab, we split the slab into different regions and calculate $g(r)$ and $S(K)$ locally. To study the signature of rings in the structural properties of the slab, we selected atoms which are part of rings of sizes 4 to 10, and calculated the static structure factor including only these atoms. Fig. 4.3 shows
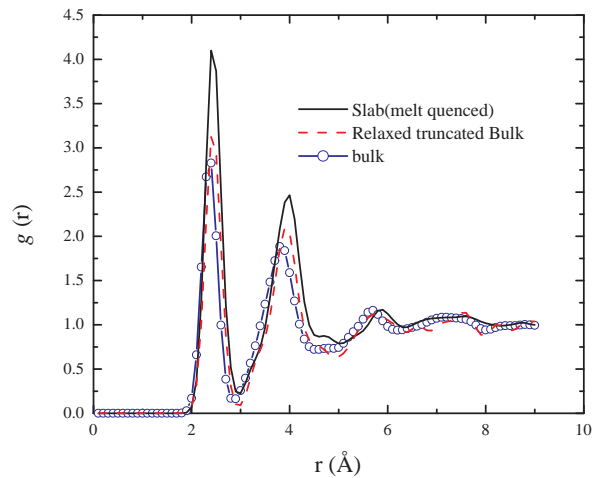
Figure 4.4: Total $g(r)$ of new slab model is compared with that of 'relaxed' truncated glass slab and bulk model.

the comparison of $S(K)$ for both sets of atoms. Atoms which are not part of these rings contribute relatively more at $K = 2.0$ Å^{-1} to the total structure factor of the slab as compared to ring atoms, while the rest of the spectrum is dominated by the contribution from the atoms which are part of rings. Fig. 4.4 shows total $g(r)$ of the melt-quenched slab, 'relaxed' slab and of the bulk model. The first peak for both the melt-quenched and 'relaxed' slab is increased to 2.44 Å and 2.43 Å respectively as compared to 2.35 Å for the bulk model. For the melt-quenched slab, heights of first and second peak is increased considerably as compared to that of relaxed truncated bulk and bulk model, which is a direct consequence of increase in the Ge-Se bonds and increase in the number of rings. Fig. 4.5 shows the contribution to the total $g(r)$ of the slab from the upper, bottom and inner regions. Increase in the height of first
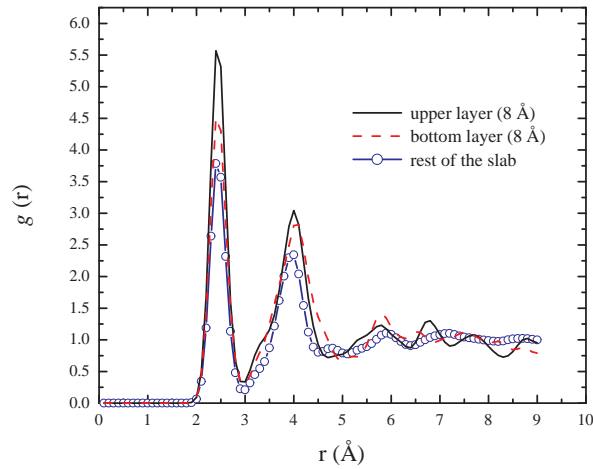
Figure 4.5: $g(r)$ of the upper bottom and interior region of the new slab model.

peak for upper and bottom layer shows an increase of Ge-Se bonds on outer layers as compared to the inner region. At larger distances these layers show some small peaks which are suppressed in the inner region. These peaks correspond to rings attached to each other. Structural analysis of the slab reveals an enhancement of atomic ordering at larger distances on outer layers due to the appearance of ring network.

4.4 Vibrational density of states and normal modes

Dynamical properties of the slab is studied by calculating the vibrational density of states (VDOS). The normal mode spectrum is determined from the dynamical matrix, which is obtained by displacing each atom by 0.03 Å in three orthogonal directions and performing first principle force calculation to obtain the force constant
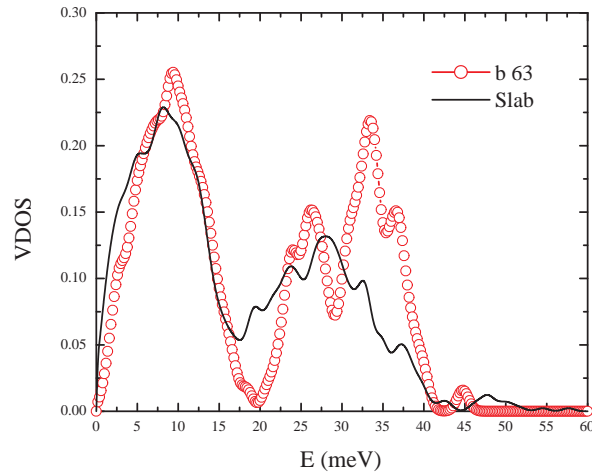
Figure 4.6: Vibrational density of states of the slab and bulk [100](63 atom) models.

matrix. Fig. 4.6 shows the vibrational density of states (VDOS) for both $GeSe_2$ bulk and slab models. The bulk model (63 atoms) is due to Cobb. et.al [100]. As compared to the VDOS of the bulk model, the middle A_1 band and the optical band is mixed for the slab, while the acoustic band follows nearly the same profile as that of bulk. The reason for this change at higher modes lies in the increase of Ge-Se bond lengths as compared to that of bulk. Higher modes are characterized by stronger localization as compared to extended lower modes. Due to the increase in the Ge-Se bond lengths, the localization of higher modes is decreased and the over all distribution weight is shifted towards the lower modes. The effect is similar to what was reported by Cobb et al.[101] for liquid bulk $GeSe_2$, which shows a similar mixing of the two bands.
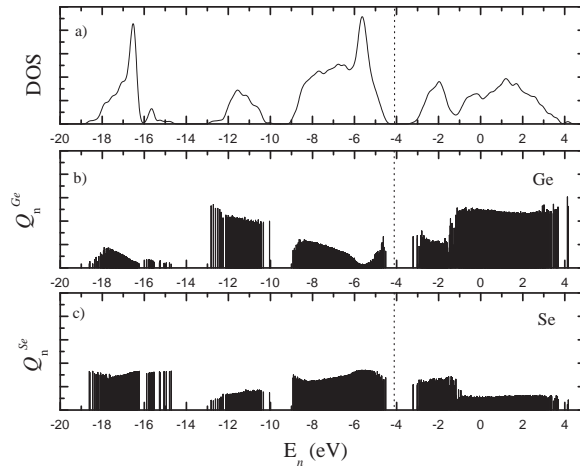
Figure 4.7: a). The EDOS for the whole slab. dotted line shows the position of fermi level. b) and c) shows the Mulliken charge on Ge and Se sites respectively.

4.5   Electronic Properties

The electronic density of states (EDOS) for the GeSe$_2$ (Fig. 4.7a) looks similar to that of bulk. In order to analyze the physical nature of eigenstates, we calculated the Mulliken charge at each atomic site for each eigenstate. For each eigenstate n, we define an average charge Q_n^α accumulated on atomic site 'α'. Fig. 4.7b and 4.7c shows the charge spectrum for Ge and Se respectively. It is interesting to note that the average charge on Ge sites is increased at valence and conduction tails, compared to Se sites. It suggests that the localization at the band tails is greatly influenced by the Ge sites. Charge on Ge sites is found to be effected by the geometrical defects. 3-fold Ge show larger average bond length 2.46 Å, as compared to 2.44 Å for 4-fold Ge, with larger angle deviations from the tetrahedra angle 109.4^o ranging from
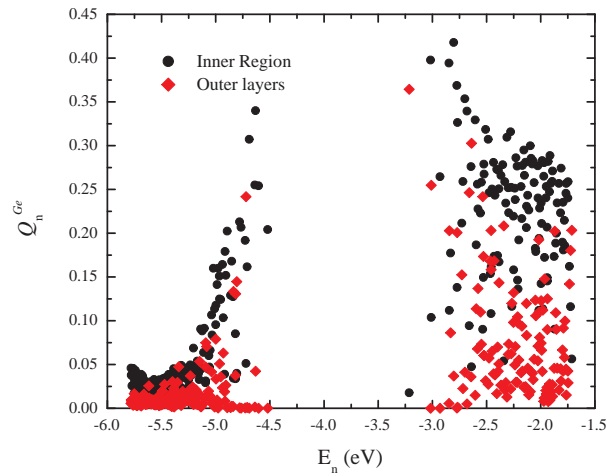
Figure 4.8: Q_n accumulated on Ge sites in outer and inner regions of the slab for valence and conduction band edges.

78° to 94°. The 3-fold Ge and their neighboring Se sites are found to be the main contributors to the total charge for valence tail eigenstates with some contribution from the 1-fold Se sites. The 4-fold Ge sites with average bond lengths ranging from 2.44 Å to 2.45 Å mainly contribute to the total charge corresponding to conduction tails.

Ge atoms on the upper and bottom layers (8 Å thickness) show more ideal co-ordination statistics. Only 24% of the total three fold Ge are present in the upper and bottom layers of the slab. As we have mentioned before, the localization at the valence tail is mostly contributed by three fold Ge, thus the surface atoms show (Fig. 4.8) less average charge accumulation for the valence tail as compared to the atoms in the interior. This decrease in the coordination defects stands in contrast to the

general understanding of crystalline surfaces, where defect density increases at the surface due to the increase in the concentration of the dangling bonds, which results in the increase in localized states. In crystalline case, surface atomic positions are less affected by the neighboring network as compared to the amorphous phase where the local network is more random and adopts more to allow the surface to minimize its energy. On the crystalline surface, atoms being less diffusive tend to settle in a local minimum energy configuration in under coordinated state. This is different in case of glassy slab obtained through annealing and quenching which allows the species to diffuse more, and thus they are able to scan the larger energy configuration space, hence settle in a better coordination state.

CHAPTER 5

Hidden Structure in Amorphous Solids

F. Inam, James P. Lewis and D. A. Drabold, Phys Stat Sol (submitted)

The continuous random network (CRN) has become the accepted model for homogeneously disordered materials, and for good reason: such atomistic models reproduce the experimentally observed properties of the materials, including some of the finer details, such as the Urbach tailing in the electronic density of states[102][22][103][14].

The understanding of the effects due to the topological disorder (broadening in bond lengths and bond angles) on the electronic properties, specially on the electronic band tails of amorphous semiconductors is an important subject from both scientific and technological point of view. The exponential nature of the band tails (Urbach tails [7]) of semiconductor amorphous solids is generally considered as an outcome of such disorder. The localized band tail states, which directly effects the optical and transport properties of the system, are found to be centered on topological defects in a wide variety of amorphous systems [8][9][97]. These observations raises questions regarding the origin of these defects and the nature of their link to the band tail states. In this spirit, a number of realistic CRN models of amorphous silicon (a-Si) are examined recently. It is reported that there are subtle topological correlations

that have not been previously noted: short bonds tend to be connected to other short bonds and an analogous statement for long bonds. In a-Si, the longer bonds form filamentary (1-D) structures, and the short bonds tend to cluster in a higher dimensional way, albeit with some 1-D character. It is also shown that the Urbach tails in the electronic density of states arise from these structures [4](the valence tail associated with the short bonds, conduction tail with long bonds).

Here we explore the case of a-Si a bit farther, and look for related phenomena in glasses (silica) and beyond. Obvious questions include: (1) Are filaments universal? (2) Do these topological features offer a general explanation for the origin of the Urbach tails? (3) Why do these structures form, and can they be manipulated to tailor the band tails in a useful way? We do not offer complete answers to these questions, but provide new information relevant to all three.

5.1 Models

For a-Si, we focus on a 512-atom model due to Djordjevic, Thorpe and Wooten (DTW)[104], made using the Wooten-Weaire-Winer (WWW) approach[102]. The DTW model is thoroughly relaxed within the WWW scheme, and to our knowledge, is not in significant contradiction with any experiment (structural, electronic or vibrational). The model has perfect four-fold coordination. We have relaxed the model with an accurate ab intio code and find tiny rearrangements, with no bond breaking or formation. We look for analogous structural and electronic correlations in a-SiO$_2$. For
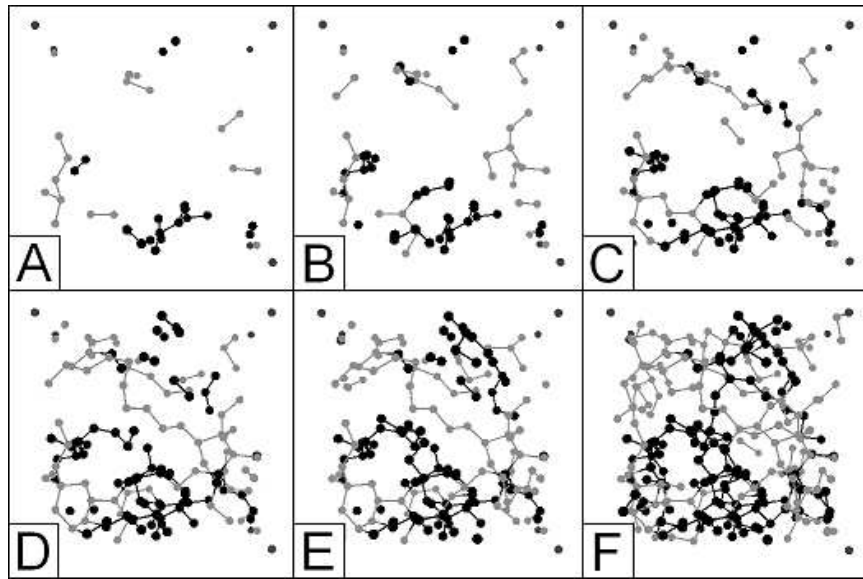
Figure 5.1: ((A) 1%, (B) 2%, (C) 3% (D) 4% (E)5% and (F) 8% longest (light) and shortest (dark) bonds in 512-atom DTW model of a-Si (from [13].)

a-SiO$_2$, we start with a 648-atom Decorate and Relax model in excellent agreement with experiment[7].

All electronic structure and force calculations are implemented with SIESTA, a standard first principles, local basis code. We updated the model of amorphous silica by relaxing it with a highly optimized double-zeta-polarized basis in SIESTA [62], kindly provided by E. Artacho. Changes were small compared to the published model.

5.2   aSi: short recapitulation

Previous work [13][14] on a-Si demonstrated that: (1) long and short bonds are spatially correlated, short favouring proximity with short, and long with long. Fur-

thermore, the long bond structures are filamentary, whereas the short bonds tend to cluster in 3-D (see Fig.5.1). (2) The electronic valence tails arise from short bonds and the conduction tails from long bonds (Fig.5.2); (3) Energies close to the Fermi level (Ef) are localized on the longest (for energies slightly above Ef) and shortest bonds (for energies slightly below Ef); (4) If the network is changed to eliminate the short-short and long-long correlations (but no bonds are broken or formed) the model does not yield a exponential density of states; (5) Simulations of relaxed point defects (Si divacancy) in diamond show a filamentary structure upon relaxation, and hint at the formation of an exponential tail, in apparent agreement with ion-bombardment experiments, that reveal the appearance of an Urbach edge before amorphization [14].

5.3   aSi: Defect Nuclei

To quantitatively characterize the long or short bonds and their associated strain or relaxation field, we look at how bond lengths vary as a function of distance from the defect centre or nucleus by this we refer to a central bond smaller (or larger) than any nearby. In Fig.5.3, we show the characteristic length of a particular short-bond cluster. Λ is the longest distance to sites with a normal bond length. We repeat this analysis for many defect nuclei.

In Fig. 5.4, we plot $\Lambda(\delta r)$, where δr is the deviation from the mean bond length in a-Si (about 2.35Å). The plots are noisy (and not to be taken seriously in any case
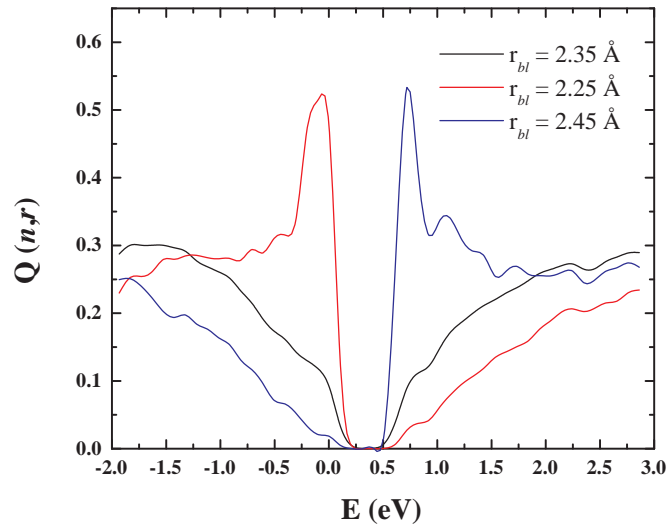
Figure 5.2: Normalized projection of q(n, r) for short, mean and long-bond lengths. The valence tail states are derived primarily from short bonds, the conduction tail states from long bonds. The mean bond length is about 2.35Å (from [14])
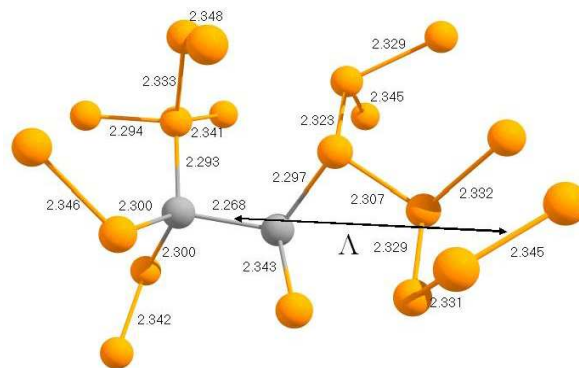
Figure 5.3: Example of a short-bond cluster in a-Si. Λ: linear extent of densified region induced by defect nucleus (grey bond).
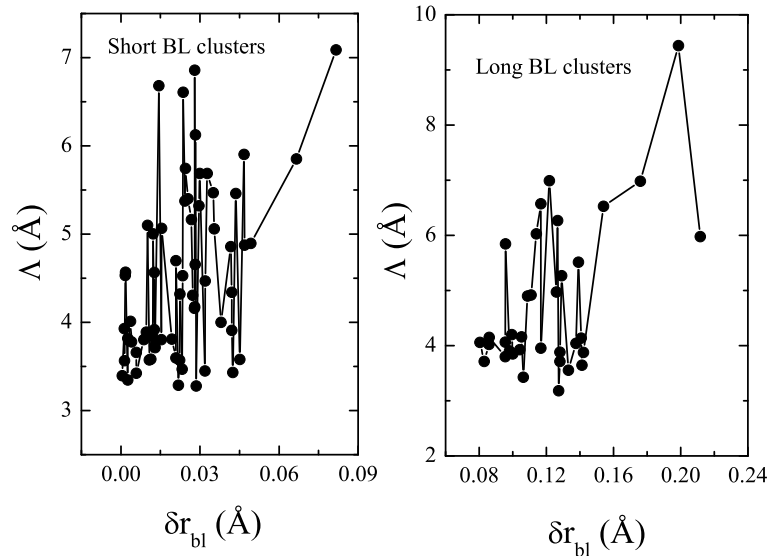
Figure 5.4: Plot of linear extent of relaxed defect Λ as a function of δr, difference in mean bond length. $\delta r < 0$ implies short bonds, $\delta r > 0$ long.

for $\delta r / f \ll 1$, where $f \sim 0.09$Å is the FWHM of the a-Si bond length distribution function), but show that for short bonds, Λ becomes large; whereas for bonds longer than the mean, there is no obvious functional dependence: long bonds do not imply a long-range relaxation field. We further differentiate between the long- and short-bond clusters by computing the number of atoms N_{cl} participating in the deformation caused by a particular nucleus (Fig. 5.5). Here, the difference between long and short bond cases is stark, reflecting the strong correlation between the relaxation around the short bond defects and the bond length deviation at the nucleus. This implies that in a-Si, the short bond is a seed for growing a local volume of higher density, and the shorter the bond the larger the effect. Roughly, this suggests that if one is able
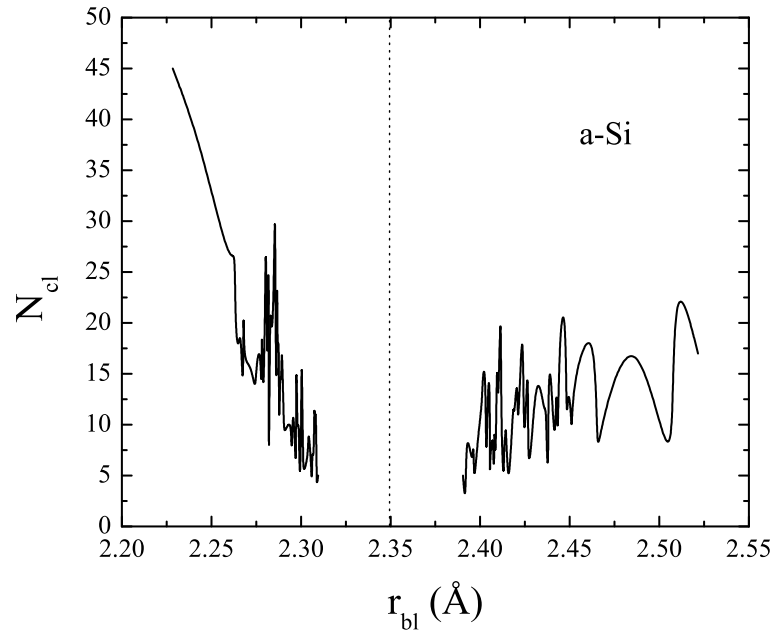
Figure 5.5: Number of atoms in short-bond and long-bond clusters (N_{cl}) are plotted agianst the central bond length of the cluster for a-Si. Mean bond length is represented by the dotted line.

to create a short bond in any fashion, one can expect the network to locally densify around that nucleus.

5.4   The Case of a-SiO$_2$

The 648-atom a-SiO$_2$ model is chemically ordered, all Si are four-fold, and all O are two-fold. The neutron structure-factor obtained from the model is in excellent agreement with experiments (as are bond angle distributions and other observables). Here we explore the network connectivity of amorphous silica using the methods of
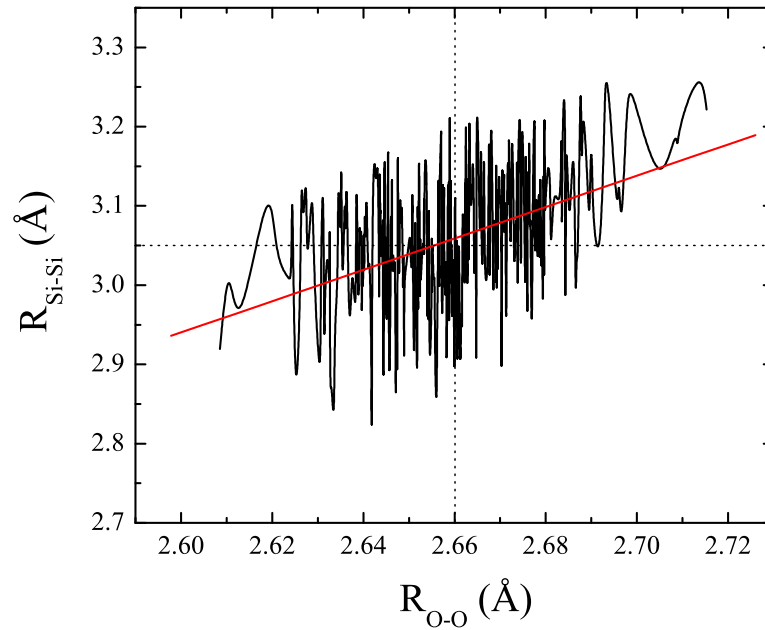
Figure 5.6: Correlation between the two lengths R_{Si-Si} and R_{O-O}. Diagonal line is a linear fit to the data. Dotted lines indicate the mean values of the two lengths.

the previous sections applied to a-Si. In contrast to a-Si, no topological correlations were found for the Si-O nearest-neighbor bond lengths. We then considered second-neighbour distances R_{O-O} (with mean length 2.66Å) and R_{Si-Si} (with mean length 3.05 Å). Since the variation in Si-O bond length is tiny (FWHM 0.01 Å), the fluctuation in R_{O-O} and R_{Si-Si} is really due to broadening associated with O-Si-O and Si-O-Si *angles*. The fluctuation in R_{Si-Si} (FWHM 0.2 Å) is larger than that of R_{O-O} (FWHM 0.1 Å). Fig. 5 indicates a linear dependence between the two lengths. The O sites with shorter R_{O-O} have shorter R_{Si-Si}, so that smaller R_{O-O} implies higher densities.

Short R$_{O-O}$ cluster
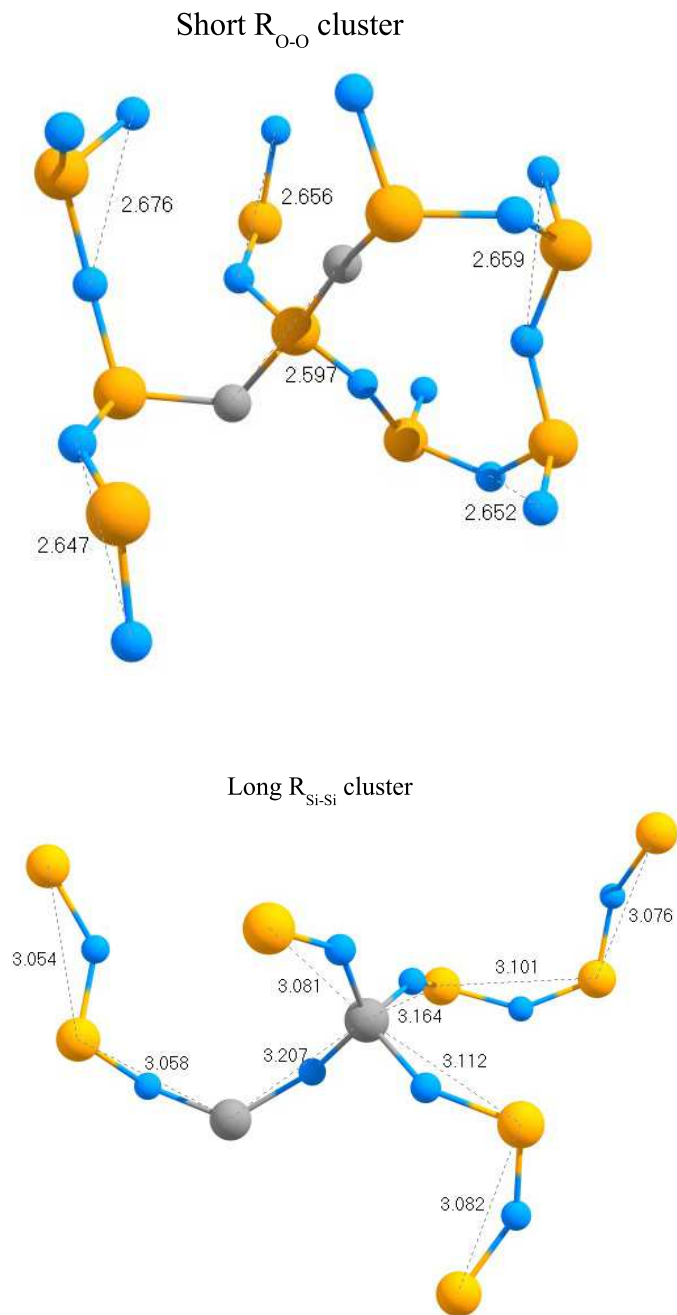
Long R$_{Si-Si}$ cluster

Figure 5.7: Examples of short R$_{O-O}$ and long R$_{Si-Si}$ clusters in a-SiO$_2$ (Si in orange and O in blue) network. Grey sites represent the defect nuclei.
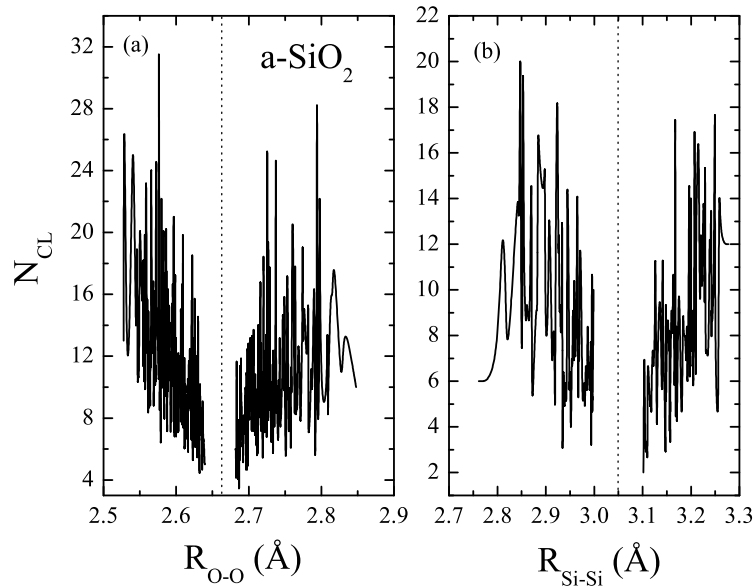
Figure 5.8: N_{cl} as a function of second-neighbor distances (see text). Vertical lines are mean-distances.

In analogy with our work on a-Si (Fig. 5.1), we show examples of the connectivity of the subnetwork formed by long and short second neighbors in Fig.5.7 . Fig. 5.8 shows the correlation between N_{cl} and the short (longer) length clusters of the two kinds. A crudely linear correlation is evident for short R_{O-O}, a trend analogous to the a-Si network. Cluster size N_{cl} also exhibits linear behavior for large R_{Si-Si}. The connectivity of short R_{O-O} clusters tends to be of a compact 3-D nature, while large R_{Si-Si} clusters are more extended and filamentary (1-D). The average spatial extension of the small RO-O clusters is of order 5.0 Å reflecting the denser nature of the surrounding network induced by the defect seed or nucleus.

The link between topology of the network and the electronic spectrum is analyzed by calculating the symmetrized charge-weighted lengths R(E) defined by:

$$R(E) = \frac{\displaystyle\sum_{l,m,n} \rho(l,n)q(l,E)q(m,E)q(n,E)}{\displaystyle\sum_{l,m,n} q(l,E)q(m,E)q(n,E)} \qquad (5.1)$$

where $\rho(l,n)$ is the distance between two second-neighbor sites 'l' and 'n' with shared site 'm' between them and 'q' is the charge computed from the electronic wave function (Kohn- Sham orbital) on a particular site for eigenenergy E. The mean deviation $\delta(E)=R(E)-R_O$, where R_O is the average length for (either R_{O-O} or R_{Si-Si}) is shown in Fig. 5.9. In addition, the inverse participation ratio (IPR), a gauge of electronic localization, is shown. An asymmetric contribution from the short R_{O-O} and long R_{Si-Si} lengths at the band tails is apparent. The localized valence tail states are clearly correlated to the short R_{O-O} lengths and localized conduction tails associated with long R_{Si-Si} second neighbor distances.

The correlation between the denser volumes, characterized by the short R_{O-O} lengths, and the valence tail states in a-SiO$_2$ system is reminiscent to the case of a-Si, and perhaps suggests a simple and broadly applicable understanding of the network origins of the Urbach edge, and the nature of the defect-induced strain field in disordered systems.
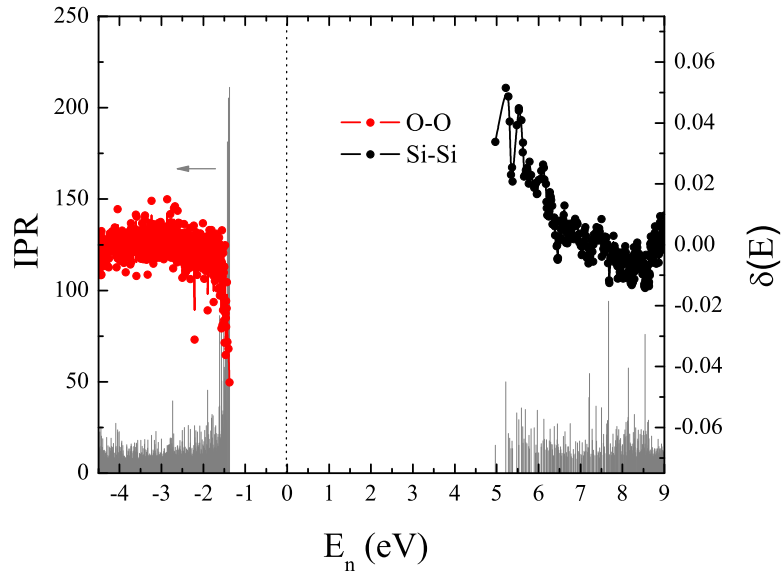
Figure 5.9: The second neighbor length decomposition of density of states. Dotted line indicates Fermi level. The valence (conduction) edge is dominated by short R_{O-O} length (long R_{Si-Si} lengths).

5.5 Farther afield

There are indications that some of the effects we report here occur (apparently) in very different systems. Thus, in the important conjugated organic compound β-carotene (C40H56) a similar tendency is observed. In Fig. 5.10, we reproduce these results. The Highest Occupied Molecular Orbital (HOMO) state and Lowest Unoccupied Molecular Orbital (LUMO) state may be viewed as molecular analogues to the valence and conduction tails, respectively. The charge-weighted bond length R(E) for the HOMO (LUMO) is 1.36 Å (1.44 Å) respectively.
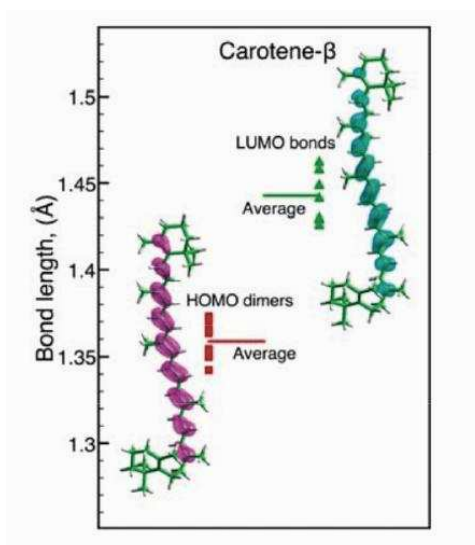
Figure 5.10: HOMO (purple) and LUMO (cyan) states correspond to short and long bonds, with mean bond length 1.36Å (1.44Å) for HOMO (LUMO).

Both experiment and computation show that the conjugation length (i.e. the number of coplanar rings in a π-system, which in turn determines the overlap strength of the π orbitals) in carotene-β is 9.7, despite the fact that there are 11 double bonds in the molecule. The HOMO orbital is tied to the shortened double bonds. Preliminary results on carotene-β suggest that frontier orbitals are localized at conjugation sites and may also contribute to lowering of the HOMO energy, compensating increase in energy due to the shortening of the double bonds (Fig. 5.10).

5.6   Discussion

The systems we have discussed here have only a few things in common. One is that all include disorder. A second feature is that all are relaxed to a minimum of suitable energy functionals (in this study, always *ab-initio*).

The consequence of a local densification around a short bond is quite plausible: the relaxation of the network around the nucleus is the strain field associated with the defect. Of course there is no similar statement for a long bond a very long bond is a broken bond; the system does not become diffuse with long bonds, it reconstructs and forms voids.

In a-Si, the decay length for the spatial correlations from a nucleus is   7Å. It is interesting that this distance is quite similar to the range of the density matrix in the material (for a review, see Ref. [105]). The latter is a measure of the spatial locality of quantum mechanics in a particular material, and also the range required of an accurate interatomic potential (specifically, the electronic contribution to the potential energy). Consistent with this observation, we note that the characteristic defect nucleus relaxation scale of a-SiO$_2$ is smaller, something like 5Å, consistent with the larger optical gap in silica, which is the prime determinant of the range of inter-atomic interactions. The observation that short bond lengths are associated with valence tail states and long with conduction states is not a surprise. Within the usual tight-binding picture, the valence states are of bonding character and the conduction states of anti-bonding character, which leads naturally to the qualitative association

of shorter bonds with valence states and longer with conduction. The following points substantially clarify this intuitive view: (1) In a purely covalent material (a-Si) the function R(E) (Eq. 1) is remarkably symmetric about E_f [13][14] (see fig.5.2); (2) the closer to Ef, the shorter (longer) the associated bonds on the valence (conduction) side of the Fermi level; (3) The short or long bonds are spatially correlated. In connection with point (3), one might suppose a priori that the short or long bonds are randomly distributed in space. If this was so, the wave functions just above or below E_f would be rather strange, with weight randomly dispersed over the network. But minimizing the energy in quantum mechanics is famously a balancing act: the electronic energy is the sum of kinetic and potential energy terms. Thus, we conclude from these calculations that the kinetic energy term, which always favours delocalization, succeeds in connecting up the long or short bonds, albeit in a 1-D fashion for the former and a higher dimension for the latter. This suggests a chicken and egg problem: Does the network organize itself (with structural blobs and filaments) to enable the electrons to reduce the Laplacian term (and delocalize electrons), or is the existence of structural blobs and filaments a consequence of minimizing the total energy (ions+electrons)? As we indicated above, it seems that some simple empirical potentials (even Keating springs) lead to structural blobs and filaments. To the extent that the empirical potentials themselves are constructed to reproduce experimental facts about the system (which in turn depend upon the electronic contribution to the total energy), perhaps the answer is not altogether clear. A key feature of electron localization is that it cre-

ates a link between an electronic energy and a structural entity in a model. Thus, we observe valence tail states (that is, energy eigenstates from a specific narrow energy range) localized on blob-like regions. An analogous statement applies to filaments for conduction tail states. This has the interesting consequence that it causes Figs. 5.8 and 5.9 to be related. In fact the quantity N_{cl} is very much like a participation ratio. This study shows that there is a close connection between R_{O-O}, R_{Si-Si} and the electronic energy E of Fig. 5.9. Thus, we show for example that dense regions in amorphous silica will particularly affect the valence tail, and lower density volumes will preferentially impact the conduction tail. From an electronic point of view the existence of blobs and filaments associated with the quantum localized-to-extended transition has been demonstrated in realistic calculations for a-Si [11]. These papers sought to characterize the localized to extended transition in a real material (with the disorder being computed from realistic structural models). They clearly showed the blob+filament nature of states near the Fermi level. The weakness of these calculations is that the models are relatively small (so far up to 10^4 atoms), whereas the 3D Anderson model has been diagonalized for systems exceeding 10^7 atoms[106]. For such large systems, it becomes possible to compute the fractal dimension for the critical eigenstates (the result is not far from D=1.3, though there continuing dispute about the exact value). Qualitatively, our work shows that on the conduction side of the Fermi level states are quite filamentary (D=1+) and on the valence side some-

thing distinctly higher, say D=3-. The value of the fractal dimension at criticality is unknown for a real system in 3D.

Finally, we note that Phillips model [107] for cuprate superconductivity emphasizes the importance of the filamentary states of the type we have detected in a-Si and a-SiO2. Interestingly, atomic-resolution tunnelling asymmetry experiments on the cuprates have observed states with topology qualitatively like what we report here [108][109]. Given the appearance of blobs and filaments (both topological and electronic) in the diverse range of systems described here, and the known importance of disorder on the properties of the cuprates, we think this work lends some support to Phillips view.

CHAPTER 6

Summary

Important results are summarized below.

1- Our work suggests that the intermediate phase in the GeSe system is associated with the competition between two stoichiometric phases (a-Se and g-GeSe$_2$). It is shown that the addition of Ge nucleates sub critical volumes of Ge clusters, which gives rise to regions of short Se chains in the network. The intermediate phase appears when most of the background a-Se network is transformed to short Se chains and the system mainly consists of small volumes of Ge tetrahedra and short Se chains. Electronic signature of such a formation of mixed phase appears as a shift in the conduction edge consistent with the XANES experiment. The models has limitations: only one set of models, hence we cannot estimate the error bars on the results of the simulation. Also, the models are of course of finite size (500 atoms), so that one may wonder about size effects. However, it must also be recognized that these calculations are based on accurate interatomic interactions, and while it is possible that details may change with additional modeling, it is highly plausible that the essential claim of tetrahedral clustering will persist.

2- we have presented a microscopic picture of Ag dynamics in the (GeSe$_3$)$_{75}Ag_{15}$ glass at low and high temperatures. It is shown that the Ag is loosely bonded to the host network and the low energy sites of Ag at 0K are at the centers of the pairs of

host sites, having distances of about 5.2 Å separating them. At low temperatures, the Ag is mainly trapped at or in between such trapping centers. At higher temperatures, the dynamics mainly consist of trapped motion followed by the hops. The trapped region of Ag consists of higher concentration of TCs forming a cage like network, which confine Ag dynamics in the cage. Large fluctuations in the concentration of TCs trigger hopping and allow the Ag to move between such cages.

3- We have modeled the g-GeSe$_2$ surface using melt-quenched method. Structural properties of the melt-quenched GeSe$_2$ slab are compared with the slab generated by the conventional relaxation technique. It is shown that the chemical ordering in the glass network is improved in the melt-quenched slab compared to the relaxed truncated bulk model. The outer layers of the GeSe$_2$ slab are mainly characterized by the rings of different sizes bundled together. Due to the increase in the Ge-Se bond length, the vibration density of states for the GeSe$_2$ slab shows a significant change for higher modes as compared to that of bulk. Electronic density of states for the GeSe$_2$ slab follows the same profile as that of bulk.

4- A farther insight into the topological-electronic correlations in a-Si a-SiO$_2$ is presented. In contrast to a-Si, tetrahedral angles (O-Si-O) in a-SiO$_2$ are found to effect the valence edge states while conduction edge states are mainly effected by Si-O-Si angles. The influence of Ge-Se-Ge angles on the conduction band of Ge$_x$Se$_{1-x}$ Glasses are discussed in chapter 2. Our work hints towards the universality of the underlying topology of the band tail states in disordered networks.

6.1   Further Exploration

Our work provides the basic understanding of the evolution of a Ge_xSe_{1-x} glassy network. It would be interesting to explore similar features in a different glass network like As_xSe_{1-x}. The atomistic picture of the IP presented is based on the clustering of Ge tetrahedra. As shown for the liquid phase, the system favors the clustering, one might look at the effects of such clustering on the cooling of the liquid phase which can provide insights into a possible link between the clustering and the glass transition in this system. For a preliminary study, long thermal trajectories (above melting point) of compositions x=0.33,0.25 and 0.20 of 400 atom size are generated.

As it is shown that the presence of Ag effects the electronic density of states around the gap, the surface models of $Ag:GeSe_3$ can be used to study the dynamics of Ag under light illumination. The study of thermal dissolution of Ag layer into the $GeSe_3$ slab is already underway. These studies may provide insights into phenomenon like photo-doping.

Using the tools developed in this study, the search for the topological-electronic correlations should be extended to the Ge-Se glasses. The goal is to explore the global features of underlying topology of the localized states in a disorder medium.

Bibliography

[1] R. Zallen, *The Physics of Amorphous Solids* (Wiley-VCH, New York, 1998).

[2] C. A. Angell, in *Insulating and Semiconducting Glasses*, edited by P. Boolchand, Series on Directions in Condensed Matter Physics, Vol. 36 (World Scientific 2000) Chap 1.

[3] W. H. Zachariasen, J. Am. Chem. Soc. **54**, 3841 (1932).

[4] N.F. Mott, Adv. in Phys. **16**, 49 (1967).

[5] J. Lucas, in *Insulating and Semiconducting Glasses*, edited by P. Boolchand, Series on Directions in Condensed Matter Physics, Vol. 36 (World Scientific 2000) Chap 11.

[6] P. W. Anderson, Phys. Rev. **109**, 1492 (1958).

[7] F. Urbach, Phys. Rev. **92**, 1324 (1953).

[8] M. Cobb, D. A. Drabold and R. L. Cappelletti, Phys. Rev. B **54** 12162 (1996).

[9] D. Tafen and D. A. Drabold, Phys. Rev. B **71** 054206 (2005).

[10] J. Dong and D. A. Drabold, Phys. Rev. Lett. **80**, 1928 (1998).

[11] J. Ludlam, S. N. Taraskin, S. R. Elliott and D. A. Drabold, J. Phys. Cond. Matter **17**, L321 (2005).

[12] R. Atta-Fynn, P. Biswas and D. A. Drabold, Phys. Rev. B **69** 245204 (2004).

[13] Y. Pan, M. Zhang and D. A. Drabold, J. Non. Cryst. Sol. **354**, 3480 (2008); see also P. A. Fedders, D. A. Drabold and S. Nakhmanson, Phys. Rev. B **58** 15624 (1998).

[14] Y. Pan, F. Inam, M. Zhang and D. A. Drabold, Phys. Rev. Lett. **100**, 206403 (2008).

[15] I. D. Aggarwal and J. S. Sanghera, J. Optoelectron. Adv. Mat. **4**, 665 (2002).

[16] M. Mitkova, in *Amorphous Semiconductors and Insulators*, edited by P. Boolchand (World Scientific Press LTD, 2000).

[17] S. R. Ovshinsky, in *Non-Crystalline Materials for Optoelectronics and devices*, edited by G. Lucovsky and M. Popescu, (INOE 2004).

[18] M. Mitkova and M.N. Kozicki, J. Non-Cryst. Sol. **299-302**, 1023 (2002).

[19] P. S. Salmon, J. Non-Cryst. Solids **353**, 2959 (2007).

[20] M. T. M. Shatnawi *et. al.*, Phys. Rev. B 77, 094134 (2008).

[21] P. Boolchand, D.G. Georgiev and B. Goodman, J. Optoelectron. Adv. Meter. **3**, 703 (2001).

[22] P. Biswas, D. N. Tafen, F. Inam, B. Cai and D. A. Drabold, J. Phys. Cond. Matter **21**, 084207 (2009).

[23] Jun Li and D. A. Drabold, Phys. Rev. B **61**, 11998 (2000).

[24] X. Zhang and D. A. Drabold, Phys. Rev. Lett. **83**, 5042 (1999).

[25] R. M. Martin, *Electronic Structure*, (Cambridge Univ. Press, Cambridge UK 2004).

[26] P. Boolchand, D.G. Georgiev and B. Goodman, J. Optoelectron. Adv. Meter. **3**, 703 (2001).

[27] D. Sharma, S. Sampath, N. P. Lalla, and A. M. Awasthi, Physica B **357**, 290 (2005).

[28] Y. Wang, E. Ohata, S. Hosokawa, M. Sakurai, and E. Matsubara, J. Non-Cryst. Solids **337**, 54 (2004).

[29] S. Hosokawa, Y. Wang, J. F. Berar, M. Skaurai, and W. C. Pilgrim, J. Non-Cryst. Solids **326327**, 394 (2003).

[30] M. Taniguchi, T. Kouchi, I. One, S. Hosokawa, M. Nakatake, H. Namatame, and K. Murase, J. Electron Spectrosc. Relat. Phenom. **78**, 507 (1996).

[31] D. I. Novita, P. Boolchand, M. Malki, and M. Micoulaut, Phys. Rev. Lett. **98**, 195501 (2007).

[32] P. Boolchand, X. Feng, D. Selvenathan and W. Bresser, in *Rigidity Theory and Applications*, (Kluwer Academic/Plenum Publishers, New York, 1999), p. 279.

[33] S. Chakravarty, D.G. Georgiev, P. Boolchand and M. Micoulaut, J. Phys. Condens. Mater. **17**, L7 (2005).

[34] A.J. Rader, B. Hespenheide, L. Kuhn and M.F. Thorpe, Proc. Nat. Acad. Sci. **99**, 3540 (2002).

[35] J.C. Phillips, Phys. Rev. Lett. **88**, 216401 (2002).

[36] Ingrid Petri, Philip S. Salmon, Phys. Rev. Lett. **84**, 2413 (2000).

[37] J.C. Phillips, J. Non-Cryst. Solids **34**, 153 (1979).

[38] J.C. Phillips, J. Non-Cryst. Solids **43**, 37 (1981).

[39] M.F. Thorpe, J. Non-Cryst. Solids **57**, 355 (1983).

[40] P. Boolchand, X. Feng and W. J. Bresser, J. Non-Cryst. Solids **293-295**, 348 (2001).

[41] M.F. Thorpe, D.J. Jacobs, M.V. Chubynsky and J.C. Phillips, J. Non-Cryst. Solids **266-269**, 859 (2000).

[42] M. Micoulaut and J. C. Phillips, Phys. Rev. B **67**, 104204 (2003).

[43] M. V. Chubynsky, M.-A. Biere and N. Mousseau, Phys. Rev. E **74**, 016116 (2006).

[44] S. Hunter, A. Bienenstock, and T.M. Hayes, in *The Structure of Non-Crystalline Materials*, edited by P.H. Gaskell (Taylor and Francis, London, 1977), p. 73.

[45] J. M. Oldale, J. Rennie, and S. R. Elliott, Thin Solid Films **164**, 467 (1988)

[46] J. H. Lee, A. P. Owens, A. Pradel, A. C. Hannon, M. Ribes, and S. R. Elliott, Phys. Rev. B **54**, 3895 (1996).

[47] J.Z. Liu and P.C. Taylor, J. Non-Cryst. Solids **114**, 25 (1989).

[48] G. Lucovsky and J. C. Phillips, J. Non-Cryst. Solids **352**, 1534 (2006).

[49] Y. Wang, M. Mitkova, D.G. Georgiev, S. Mamedov, P. Boolchand, J. Phys. Condens. Matter **15**, S1573 (2003).

[50] M. Kawasaki, J. Kawamura, Y. Nakamura and M. Aniya, Solid State Ionics **123**, 259 (1999).

[51] M.A. Urena, A.A. Piarristeguy, M. Fontana and B. Arcondo, Sol. State Ionics, **176** 505 (2005).

[52] E. Bychkov, A. Bychkov, A. Pradel and M. Ribes, Sol. State Ionics, **113-115**, 691 (1998).

[53] E. Bychkov, V. Tsegelnik, Yu. Vlasov, A. Pradel and M. Ribes, J. Non. Cryst. Sol. **208**, 1 (1996).

[54] Chad Holbrook, Ping Chen, D. I. Novita, and P. Boolchand, IEEE Trans. Nanotechnol. **6**, 530 (2007).

[55] M. Mitkova and M. N. Kozicki, in *Optoelectronic Amorphous Materials and Devices*, edited by G. Lucovsky and M. Popescu, (INOE Publ. House 2004).

[56] M. N. Kozicki, M. Park and M. Mitkova, IEEE Trans. Nanotech. **4**, 331 (2005).

[57] M. N. Kozicki, Maria Mitkova, J. Non-Cryst. Solids **352**, 567 (2006).

[58] D. N. Tafen, D. A. Drabold and M. Mitkova, Phys. Rev. B **72**, 054206 (2005).

[59] D. N. Tafen, D. A. Drabold and M. Mitkova, Phys. Stat. Sol. B **242**, R55 (2005).

[60] O. F. Sankey and D. J. Niklewski, Phys. Rev. B **40**, 3979 (1989); J. P. Lewis, K. R. Glaesemann, G. A. Voth, J. Fritsch, A. A. Demkov, J. Ortega, and O. F. Sankey, Phys. Rev. B **64**, 195103 (2001); P. Jelinek et al., Phys. Rev. B **71**, 235101 (2005).

[61] G. Kresse and J. Furthmuller, Phys. Rev. B **54**, 11169 (1996).

[62] E. Artacho, E. Anglada, O. Dieguez, J. D. Gale, A. Garcia, J. Junquera, R. M. Martin, P. Ordejon, J. M. Pruneda, D. Sanchez-Portal and J. M. Soler, J. Phys. Condens. Matter **20**, 064208 (2008)

[63] F. Inam, M. T. Shatnawi, D. N. Tafen, S. J. L. Billinge, P. Chen, and D. A. Drabold, J. Phys.: Condens. Matter **19**, 455206 (2007).

[64] Takeshi Egami and S. J. L. Billinge, *Underneath the Bragg peaks*, (Elsevier, 2003).

[65] W. Bresser, P. Boolchand and P. Suranyi, Phys. Rev. Lett. **56**, 2493 (1986).

[66] P. Boolchand, P. Chen, M. Jin, B. Goodman and W. J. Bresser, Physica B-Condensed Matter **389**, 18 (2007).

[67] Y.Wang, O. Matsuda, K. Inoue, O. Yamamuro, T. Matsuo, and K. Murase, J. Non-Cryst. Solids bf 232234, 702 (1998).

[68] C. Patrick royall, Stephen R. Williams, Takehiro Ohtsuka and Hajime Tanaka, Nature Mater. **7** 566 (2008).

[69] D. Selvanathan, W. J. Bresser and P. Boolchand, Phys. Rev. B **61** 15061 (2000).

[70] F. Wang, P. Boolchand, K. A. Jackson and M. Micoulaut, J. Phys.: Condens. Matter **19** 226201 (2007).

[71] Results were insensitive near this range; the band shift was rigid for several eigenvalues (see Ref. [63]).

[72] F. Inam, Gang chen, D. N. Tafen and D. A. Drabold, in *Rigidity and Boolchand Intermediate Phases in nanomaterials*, (INOE, Bucharest 2009).

[73] P. Boolchand, X. Feng, and W. J. Bresser, J. Non-Cryst. Solids **293** - **295**, 348 (2001).

[74] M. N. Kozicki, Maria Mitkova, J. Non-Cryst. Solids **352**, 567 (2006).

[75] A. V. Kolobov and S. R. Elliott, Adv. Phys. **40**, 625 (1991).

[76] S.R. Elliott, J. Non-Cryst. Solids **172-174** 1343 (1994).

[77] H. Iyetomi, P. Vashishtha, and R. K. Kalia, J. Non-Cryst. Solids **262**, 135 (2000).

[78] J. C. Phillips, Rep. Prog. Phys. **59** 1133 (1996).

[79] St. Adams and J. Swenson, Phys. Rev. Lett. **84**, 4144 (2000).

[80] E. R. Weeks, D. A. Weitz Phys. Rev. Lett. **89**, 0957704 (2002).

[81] J. Habasaki, I. Okada, Y. Hiwatari, Phys. Rev. B **55**, 6309 (1997).

[82] J. Habasaki, Y. Hiwatari, Phys. Rev. E **59**, 6962 (1999).

[83] J. Habasaki, K.L. Ngai, Y. Hiwatari, Phys. Rev. E **66**, 021205 (2002).

[84] FIREBALL did not include polarization orbitals; VASP uses an essentially complete basis.

[85] D. A. Drabold, T. A. Abtew, F. Inam, Y. Pan, J. Non-Cryst. Solids, **354**, 2149 (2008).

[86] P. Tronc, M. Bensoussan, A. Brenac and C. Sebenne, Phys. Rev. B **8**, 5947 (1973).

[87] P. M. Bridenbaugh, G. P. Espinosa, J. E. Griffiths, J. C. Phillips and J. P. Remeika, Phys. Rev. B **20**, 4140 (1979).

[88] P. Boolchand, J. Grothaus, W. J. Breser and P. Suanyi Phys. Rev. B **25**, 2975 (1982).

[89] Murat Durandurdu and D. A. Drabold, Phys. Rev. B **65**, 104208-1 (2002).

[90] I. Rusman, L. Klibanov, L. Burstein, Yu. Rosenberg, V. Weinstein, E. Ben-Jacob, N. Croitoru and A. Seidman, Thin Solid Films **287**, 36 (1996).

[91] J. Herion, K. Szot, Ch. Ross and F. Siebke, J. Non. Cryst. Sol **227-230**, 78 (1998).

[92] S. M. Levine and S. H. Garofalini, J. Chem. Phys. **86**, 2997 (1987).

[93] G. P. Feuston and S. H. Garofalini, J. Chem. Phys. **91**, 564 (1989).

[94] S. P. Adiga, P. Zapol and L. A. Curtiss, Phys. Rev. B **74**, 064204 (2006).

[95] K. Kilian, D. A. Drabold and J. B. Adams, Phys. Rev. B **48**, 17393 (1993).

[96] G. Fabricius, E. Artacho, D. Sánchez-Portal, P. Ordejón, D. A. Drabold and J. M. Soler, Phys. Rev. B **60**, R16283 (1999).

[97] J. Dong and D. A. Drabold, Phys. Rev. B **57**, 15591 (1998).

[98] R. Haerle, G. Galli and A. Baldereschi, Appl. Phys. Lett. **75** 1718 (1999).

[99] X. Zhang and D. A. Drabold, Phys. Rev. B **62**, 15695 (2000).

[100] R. L. Cappelletti, M. Cobb, D. A. Drabold and W. A. Kamitakahara, Phys. Rev. B **52**, 9133 (1995).

[101] M. Cobb and D. A. Drabold, Phys. Rev. B **56**, 3054 (1997).

[102] F. Wooten, K. Winer and D. Weaire, Phys. Rev. Lett. **54**, 1392 (1990).

[103] J. Dong and D. A. Drabold, Phys. Rev. Lett. **80**, 1928 (1998).

[104] B.R. Djordjevic, M.F. Thorpe and F. Wooten, Phys. Rev. B **52**, 5685 (1995).

[105] D. A. Drabold, Eur. Phys. J. B **68**, 1 (2009); X. Zhang and D. A. Drabold, Phys. Rev. B **63**, 233109 (2001).

[106] O. Schenck, O. Bollhofer and R. A. Romer, SIAM Review **50**, 91 (2008).

[107] J. C. Phillips, Phys. Rev. B **75**,, 214503 (2007), and references therein.

[108] Y. Kohsaka et al., Science **315**, 1380 (2007).

[109] M. C. Boyer et al. Nature Physics **3**, 802 (2007).

Appendix A

Surface of a solid electrolyte:

$(GeSe_3)_{0.9}Ag_{0.1}$

An alternate method is applied to model the solid electrolyte surface. For the $GeSe_3$:Ag surface, we first cut the large 500 atom bulk model of $GeSe_3$ [chapter 2] into half in z direction to obtain a large surface area (24.621×24.621 Å^2) in the xy-plane. The truncated bulk is then equilibrated using code FIREBALL (with approximations same as mentioned in chapter 4) at 450K for about 10 ps and then at 300K for 5 ps to obtained a slab model of $GeSe_3$ composition at the room temperature. During equilibration, atoms in the upper and bottom layers (5 Å) were displaced about 4.0 Å on average from their initial positions. In the middle region, the average displacement of about 1.5 Å is observed. This shows a considerable reconstruction of the network at the upper and bottom layers. The width of the resulting slab is about 17 Å. As discussed in chapter 3, the Ag trapping sites are the centers of two glass network sites with a distance of about 5.0 Å in between them. We randomly selected such pair configurations in the slab and introduced 10% Ag at their centers (atoms present in the cell are 62 Ge, 186 Se and 27 Ag). The system is equilibrated at 300k for 25 ps and then cooled to 0K. The resultant slab is then relaxed to reduce forces to below 0.02 Å/eV. Fig. A.1 shows the slab configuration. The Ge sites are mostly clustered
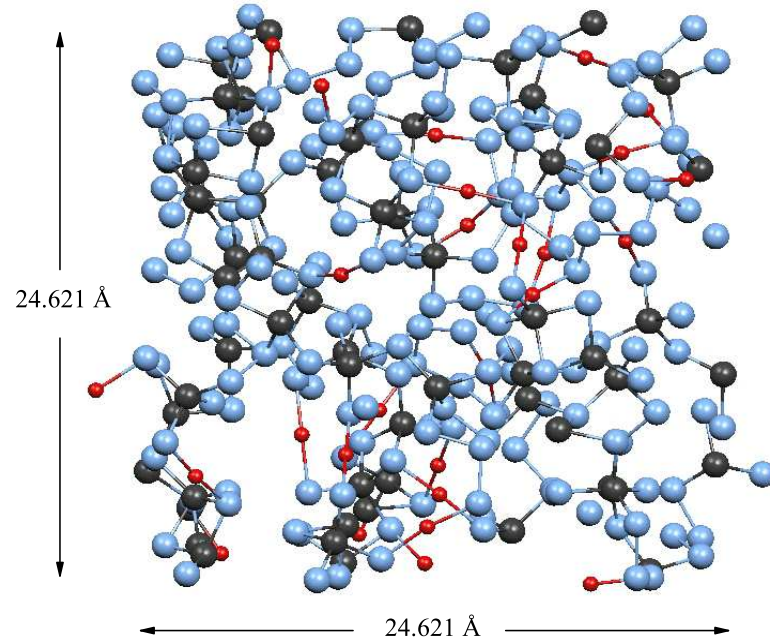
Figure A.1: $(GeSe_3)_{0.9}Ag_{0.1}$ slab configuration. Ge and Se sites are shown in black and blue respectively. Ag are in red. The surface has a large square area with a side 24.621 Å in xy-plane.

together with Se present between them, a trend similar to the bulk $Ge_{1-x}Se_x$ models (chapter 2). The Se rich region consists of short Se chains. The Ag sites are mainly present in the Se rich region due to the peculiar geometry of the trapping sites of Ag. The bonding configuration of Ag is similar to that in the bulk (chapter 3), i-e. at the center of two network sites about 5.0 Å distance apart. Interestingly, the addition of Ag to the $GeSe_3$ didn't bring any considerable topological change in the glass network. Only the angles around Ag sites are readjusted such that all the Ag have only 2
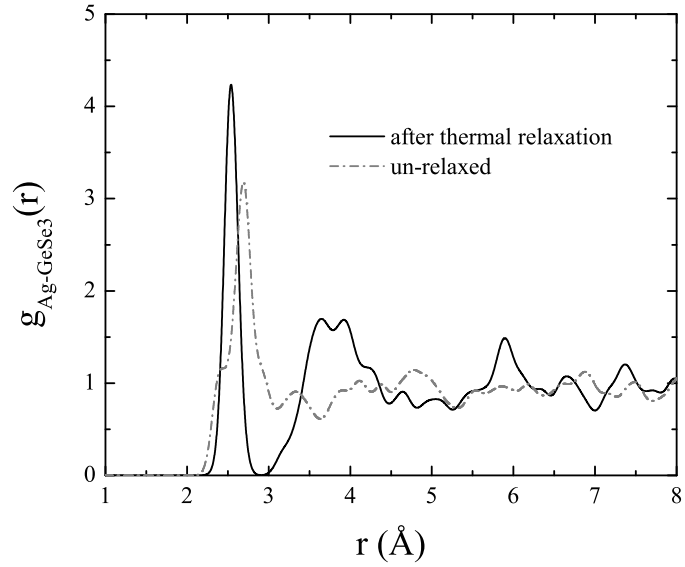
Figure A.2: The partial pair correlation function $g_{Ag-GeSe_3}(r)$ between Ag and GeSe$_3$ glass network.

neighbors within a radius of 3.0 Å, compared to an average coordination of 3.3 in the un-relaxed cell. It suggests that, if permitted, Ag would tend to keep its coordination to 2. Fig. A.2 shows the partial pair correlation function $g_{Ag-GeSe3}(r)$ between Ag and the glass network, before and after relaxation. After thermal relaxation, a well defined first neighbor shell has emerged with a first minimum at 2.8 Å and a second neighbor shell between 3.0 and 4.5 Å.